Enhancing Laser-Driven Ion Acceleration through Computational Methods

DISSERTATION

Presented in Partial Fulfillment of the Requirements for the Degree Doctor of Philosophy in the Graduate School of The Ohio State University

By

Ronak Desai, B.S., M.S.

Graduate Program in Physics

The Ohio State University

May 2025

Dissertation Committee:

Professor Chris Orban, Advisor

Professor Douglass Schumacher

Professor Alexandra Landsman

Professor Brian Skinner

Abstract

An abstract goes here. It should be less than **500 words**.

Dedicate to ...

Acknowledgments

I want to thank ...

Vita

May, 2019	B.S. Physics, B.A. Mathematics, Rowan University, Glassboro, NJ
August 2020 - July 2021	Graduate Fellow, The Ohio State University, Columbus, OH
August 2021 - April 2023	Graduate Teaching Associate, The Ohio State University, Columbus, OH
August, 2023	M.S. Physics, The Ohio State University, Columbus, OH
August 2023 - July 2025	Graduate Research Associate, The Ohio State University, Columbus, OH

Publications

Applying Machine Learning Methods to Laser Acceleration of Protons: Lessons Learned from Synthetic Data

Towards Automated Learning with Ultra-Intense Laser Systems Operating in the kHz Repetition Rate Regime

Intelligent Control of MeV Electrons and Protons

Can Two Pulses Enhance Proton and Electron Acceleration?

Fields of Study

Major Field: Physics

Table of Contents

Appendices

List of Figures

Figure **Page**

List of Tables

Acronyms

AFIT Air Force Institute of Technology. 45

ALLS Advanced Laser Light Source. 5

BO bayesian optimization. 36

CCD charge coupled device. 62

CSUCI California State University - Channel Islands. 45

EDX energy dispersive x-ray fluorescence. ix, 6

eTNSA enhanced target normal sheath acceleration. 22, 29, 31–33

GPR gaussian process regression. 45, 46, 51, 52

GPU Graphics Processing Unit. 46, 52, 61

HEDS high energy density science. 36

IBA Ion Beam Analysis. 5

IMPT intensity modulated proton therapy. 2

LANL Los Alamos National Laboratory. 5

LLE Laboratory for Laser Energetics. 5

LLNL Lawrence Livermore National Laboratory. 20, 29

LSP Large Scale Plasma: An implicit particle-in-cell code. 27

LWFA laser wakefield acceleration. 23

MAPE Mean Absolute Percentage Error. xi, 46–48, 52, 53, 59

ML machine learning. xi, 36, 37, 45–49, 53, 56, 58, 59

NGP nearest grid point. 25

NIF National Ignition Facility. 5

NIF-ARC National Ignition Facility - Advanced Radiographic Capability. 4, 5

NN neural network model. 36, 45, 46, 51–53, 56, 59

OMEGA-EP OMEGA Extended Performance System. 5

OSC Ohio Supercomputer Center. 46

OSUCCC The Ohio State Comprehensive Cancer Center. 2

PIC particle-in-cell. x, 24, 26, 29–31, 33, 36, 74

POLY polynomial regression. 52, 53, 56

RBF Radial Basis Function. 46

RF radio frequency. 5

RMSE Root Mean Squared Error. 56

RPA radiation pressure acceleration. 22

SOBP spread-out Bragg peak. 2

SRIM stopping range of ions in matter. 2

SVGP stochastic variational gaussian process. 52, 53, 56, 59

SVR Support Vector Regression. 45, 46, 51, 52

TNSA target normal sheath acceleration. x, 5, 6, 19–22, 29, 31, 33, 42, 74

WP-ELL Extreme Light Laboratory at the Wright-Patterson Air Force Base. 37, 45, 51, 60

XPIF x-ray and particle-induced fluorescence. ix, 5, 6

Chapter 1
Introduction

1.1 Lasers for Particle Acceleration

Explain what a laser stands for, stimulated emission, lasing medium, what the Ti:sapphire crystal does and why it is chosen, CPA

1.1.1 Chirped Pulse Amplification

1.1.2 ...

1.2 Applications

This section highlights some of the most important applications of laser-based proton accelerators that motivates much the projects I have worked in during my PhD studies: (1) proton therapy for cancer treatment, (2) proton radiography for imaging, and (3) ion beam analysis for materials characterization.

1.2.1 Proton Therapy

Due to having no cure, cancer is one of the largest medical challenges faced worldwide and generally requires the use of harsh treatments like invasive surgery, chemotherapy, and immunotherapy. Another relevant treatment is called radiotherapy and more than half of all people with cancer will receive it as a part of their medical care [20]. Typically, a large machine will provide a source of x-rays (a type of energetic ionizing radiation) that kills the tumor. However, this radiation does not discern whether the cells are cancerous or not – healthy tissue along the radiation beam path surrounding the tumor will also be damaged. This damage can be mitigated by shooting many beams from different angles such that they overlap at the site of the tumor. In this way, the dose delivered in the beam overlap region will be significantly higher than the surrounding tissue. This approach is typically employed by situating the machine on a rotating "gantry"

As early as 1905, Bragg [21] identified that charged particles have different properties than x-rays when passing through matter. Specifically, he identified that radium particles lost more energy (i.e. delivered a higher dose) at a lower speed. Physically, the slower the radium particles, the more time it has to interact with each of the individual atoms and the more energy it can deposit. This means that when the radium first enters a material at its highest speed, it is losing energy slowly in contrast to when it is at a slow speed and about to stop it is losing energy very quickly. In 1946, Wilson [22] identified that this property of charged particles would enable a more concentrated dose to be delivered closer to the site of a tumor. In Figure 1.1, these differences are explicitly highlighted between x-rays and proton beams traveling through water. It can be seen that the proton beam is sharply peaked at a particular distance of around 23 centimeters, where the x-ray beam delivers a relatively higher dose at just a few centimeters. One can see the advantage of protons quite readily from this picture – if a tumor is located 23 centimeters into the body, the protons, comparatively to the x-rays, will deliver more energy at the tumor site and less energy to the surrounding tissue. The shape of the proton beam curve in this graph is appropriately referred to as a "Bragg Curve" which peaks at the "Bragg Peak".

The specifics of the depth-dose curve depend on the material that the particles are traveling through as well as initial energy of the protons. These conditions are well-studied by empirical measurements of the stopping range of ions in matter (SRIM) [23] and can be combined with other techniques to achieve a depth-dose curve that not only peaks at different depths, but also has a spread-out Bragg peak (SOBP) that expands the region where the highest dose is delivered. The most modern form of proton therapy is called intensity modulated proton therapy (IMPT) whose intensities are modulated to optimally balance tumor dose and sparing of normal tissues [1]. The first proton therapy center opened at the Loma Linda University Medical Center in California in 1990, but today there are more than 100 centers around the world with more that are planned or in the process of construction [1].

Right here in Columbus, The Ohio State Comprehensive Cancer Center (OSUCCC), in collaboration with Nationwide Children's Hospital opened a 55,000 square foot proton therapy center in December of 2023 [24] that uses IMPT. Despite all the aformentioned benefits of proton therapy, the intial cost is tremendous – OSUCCC was a 100 million dollar investment. The significant cost demonstrates the value this could bring to Central Ohio. The facility is even outfitted with the capability to perform FLASH therapy – a newer, experimental form of proton therapy that can be delivered in seconds that is still in clinical trials [24] – which shows the continued investment and innovation in this field.

The cost, however, cannot be overlooked. The conventional cyclotron accelerators used to accelerate the protons are extremely large and expensive. In recent years, it has been proposed that laser-based particle accelerators could be used to generate high energy protons.

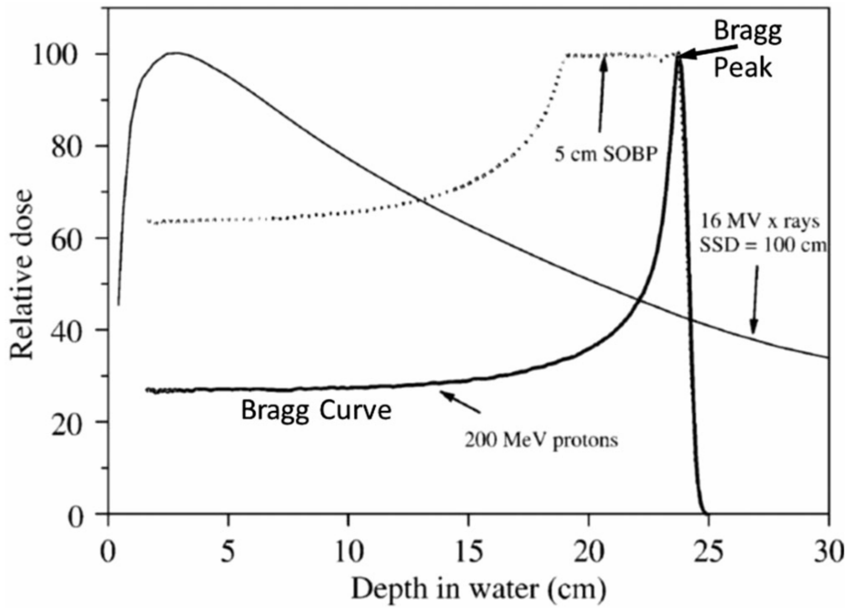

Figure 1.1: The dose delivered as a function of depth traveled in water for two types of beams are depicted – 200 MeV protons and 16 MV x-rays. Taken from Figure 1 in Mohan [1].

These facilities could in principle be smaller and less costly, but the technology is not adequately matured to be considered in the near future [25]. Laser-based sources are typically only able to generate protons in the 10s of MeV reliably (as opposed to the 100s of MeV required for clinical operation), possess orders of magnitude smaller numbers of protons, and poor reproducibility of the laser pulse output. In addition, the conventional accelerators have already made significant strides in terms of reducing cost, increasing beam quality, and reducing size in recent years [25] which is something laser-based sources will need to keep up with in the future. However, the potential of developing a smaller and lower cost proton accelerator remains an important motivating factor for many laser-plasma physicists for the coming years.

1.2.2 Proton Radiography and Laser Fusion

All of us are familiar with the use of visible light to image things. A camera's flash will send out a burst of light and the camera will record the light reflected off an object to image it. Other frequencies of light not visible to the naked eye are used all the time to image things as well. High frequency sources like x-rays are used at the dentist due to their ability to probe matter within your body. Radio waves reflect well off of electrically conductive materials like the metals in vehicles which make them ideal for military applications. In an

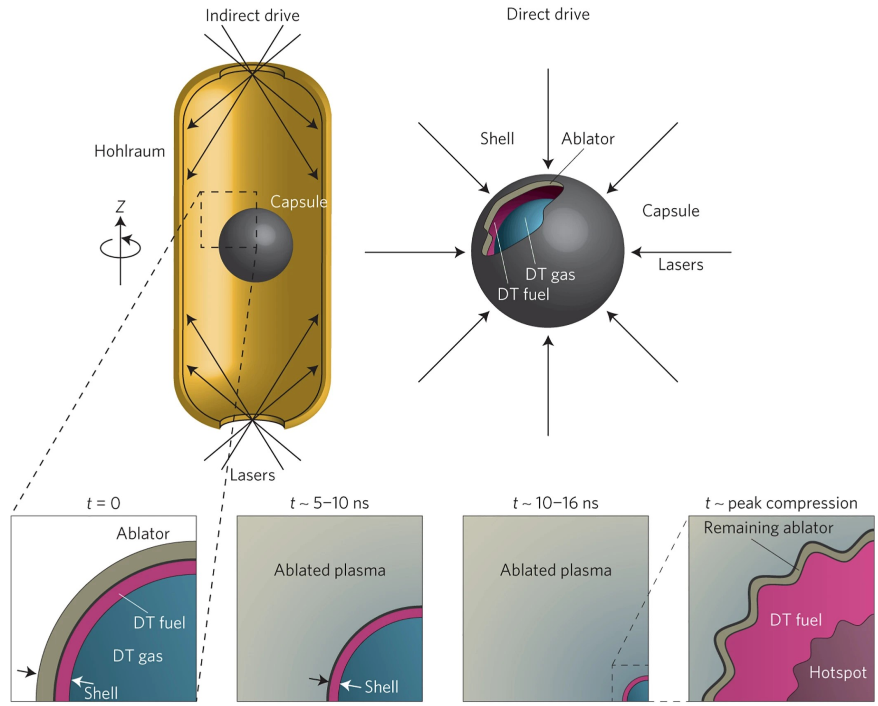

Figure 1.2: Visualization of two different approaches to laser fusion are depicted at the top. Lasers can irradiate the inside of a hollow gold can (called a hohlraum) to indirectly heat a fusion capsule or instead directly heat it. At the bottom, multiple stages of the fusion process are depicted including capsule ablation, compression, and burn. Taken from Figure 1 of Betti et al. [2].

similar way, particles can be used to image objects by analyzing how they interact. Electron microscopes have been used extensively in the past century to image materials at a much higher resolution than an ordinary visible light microscope. From Figure 1.1, we know that protons interact with matter in a different way than electromagnetic radiation like x-rays. These differences can be exploited to image things that cannot be done well with other types of radiation [26]. To give one example, a proton is a charged particle that gets deflected by electric and magnetic fields which can enable scientists to obtain information about these fields in a way that x-rays cannot.

One example of proton radiography using laser-accelerated protons is through the National Ignition Facility - Advanced Radiographic Capability (NIF-ARC). As it's name implies, NIF-ARC is typically used as light source to collect radiograph images of laser fusion experiments at NIF. These fusion experiments involve using a high powered lasers to compress a millimeter sized frozen pellet of hydrogen fuel (specifically, heavier isotopes of hydrogen called deuterium and tritium) to such high temperatures and pressures that the atomic nuclei fuse together into helium. The sun is an example of a high temperature and pressure environment that is able to sustain fusion as its vast source of energy, but we must be a little bit more clever on Earth to obtain conditions like that of in the core of our sun. A similar capability to NIF-ARC exists at the Laboratory for Laser Energetics (LLE)'s OMEGA Extended Performance System (OMEGA-EP). The OMEGA-EP provides diagnostics for the main OMEGA laser which performs fusion experiments by directly irradiating a fusion pellet. This is in contrast to the National Ignition Facility (NIF) which indirectly compresses a fusion pellet by first irradiating a gold can that surrounds the pellet. These approaches are aptly called indirect and direct drive fusion and are depicted in Figure 1.2. Proton radiography has been demonstrated successfully at the NIF through NIF-ARC [27] and at OMEGA through OMEGA-EP [28] through TNSA proton beams produced from laser-irradiated metallic foils.

Conventional sources of protons for radiography purposes are from linear accelerators like the pRad at Los Alamos National Laboratory (LANL). LANL uses radio frequency (RF) waves of around 200 MHz to accelerate particles up to 800 MeV (SOURCE). The limitation of conventional RF accelerators is the relatively low frequency. If we take the reciprocal of 200 MHz, we find that the separation between individual waves (the period) is around 5 nanoseconds. This may seem like a short time, but on the scale of femtosecond and picosecond ultra-intense pulses, this is a thousand or a million times longer! If one wanted to take proton radiographs of some experiment happening on a picosecond timescale, the conventional accelerator would not work. On the other hand, lasers typically used for laser-plasma experiments are in the infrared and have wavelengths of around 1 micron. A quick calculation tells us that the period is only around 3 femtoseconds. Since the lasers are pulsed at 3 femtoseconds, the emitted protons would also be pulsed at 3 femtoseconds which would theoretically allow us to capture 1 proton radiograph every 3 femtoseconds. Another advantage of these laser-accelerated proton beams is that they are emitted from a very small spot, on the order of microns, which is beneficial for obtaining a higher quality image [26].

1.2.3 Materials Characterization

While protons can generate images through radiography, they can also more generally tell us information about materials as a whole through a process called Ion Beam Analysis (IBA). IBA allows scientists to probe material composition and surface structures with MeV ion beams which are appealing partly due to their non-destructive nature (comparatively to sources like x-rays) [29]. IBA is currently implemented through old Van de Graaf and Tandem accelerator technology, but Passoni [29] argues that TNSA proton beams can achieve the same result in a more compact, portable, and cheaper setup.

As a proof of principle, Boivin [3] used TNSA beams from the Advanced Laser Light Source (ALLS) laser facility in Canada to perform XPIF to determine the elemental mass

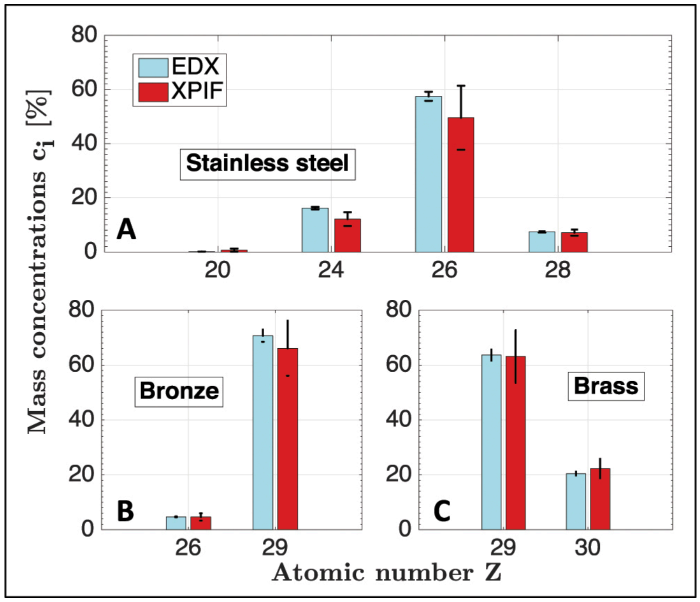

Figure 1.3: Mass concentrations of three metal alloys are shown using two different techniques: EDX and XPIF. Taken from Figure 4 of Boivin et al. [3].

concentrations of three different metal alloys: stainless steel, bronze, and brass. This is compared to a method called EDX used in conjunction a conventional mono-energetic electron beam and shown in Figure 1.3. Although XPIF has larger error bars than EDX, both methods find good agreement with each other.

As a final point, TNSA beams can be accompanied by other radiation sources like electrons, x-rays, and neutrons. Different materials characterization process could, in principle, be used in conjunction with each other. While TNSA beams are not the most common way to characterize materials today, they may emerge as an important tool for their ability to be pulsed at a high repetition rate and generated from a relatively compact system.

1.3 This Work

Talk about prior work

Talk about motivating question

Talk about how work is organized.

Chapter 2
Laser-Plasma Interactions and Ion-Acceleration

2.1 Plasma Physics

Chen [30] describes a plasma as

> a *quasineutral* gas of charged and neutral particles which exhibits *collective behavior*

In this section, the quasineutrality and collective behavior of plasmas will be discussed. One way to create a plasma is through the interaction of matter with an energetic laser. The laser has enough energy to ionize atoms to a hot dense soup that satisfy the definition of Chen. Plasmas do exist in other contexts, like those found in stars and various astrophysical systems, but these will not be explained in detail in this section. Here, we'll overview the physics of gaussian laser beams, particle motions in electric fields, and the properties of plasmas.

2.1.1 Gaussian Laser

In order to heat up a material with a laser efficiently, the energy would ideally be concentrated to a small point. Lasers are a coherent source of light that can be focused to narrow beams. The intended output of many lasers have an electric field described by the fundamental transverse electromagnetic mode [31] (TEM_{00}) described by the following electric field

$$E(r,x) = E_0\hat{y}\frac{w_0}{w(x)}\exp(-\frac{r^2}{w(x)^2})\cos(kx - \arctan(x/x_R) + \frac{kr^2}{2R(x)}) \tag{2.1}$$

where $\hat{x}$ is the propagation direction, $\hat{y}$ is the polarization direction, and $r = \sqrt{y^2+z^2}$ is the radial distance away from the laser axis. In the cosine function, $R(z) = z[1+(z_R/z)^2]$ is the radius of curvature and $\arctan(z/z_R)$ is the guoy phase. For our purposes, these won't have too much relevance. Additionally, the beam radius w is expressed as

$$w(z) = w_0\sqrt{1 + (z/z_R)^2} \tag{2.2}$$

and has a minimum value at the *beam waist* $w(0) \equiv w_0$ at the focal position of the laser. The length scale over which the beam can propagate without diverging significantly is the *Rayleigh range* $x_R \equiv \frac{\pi w_0^2}{\lambda}$. The peak intensity is related to the electric field by $I_0 = \frac{1}{2}\epsilon_0 c E_0^2$ and eq. (2.1) shows that the intensity decays as $I(x,r) = I_0(w_0/w(x))^2 \exp(-2r^2/w(x)^2)$ with increasing r and x. If we integrate this intensity distribution over the entire $y-z$ plane, we obtain the peak power $P_0 = \frac{\pi\omega_0^2}{2} I_0$. Furthermore, we can integrate the power over the pulse duration (assuming the pulse has a $sin^2(t)$ envelope) to obtain the total energy in the pulse

$$E = \frac{\pi\omega_0^2}{2} I_0 \tau_{\text{fwhm}} \tag{2.3}$$

where τ_{fwhm} is the full-width half-max and is equal to half the pulse duration for a $sin^2(t)$ pulse envelope.

2.1.2 Single Particle Motions

Electrostatics is governed by the Maxwell's equations which describe the allowed wave-like solutions for electric and magnetic fields in both matter and vacuum. The most relevant equation in this section is Gauss' Law or Poisson's Equation which can be expressed as

$$-\nabla^2\phi = \nabla \cdot \vec{E} \equiv \frac{\rho}{\epsilon_0} \tag{2.4}$$

which relates the electrostatic potential ϕ or electric field E to the charge density ρ. This equation highlights how electric fields are directed radially outward from positive charges and inward towards negative charges. The motion of an electron in the influence of an electric field E or magnetic field B is given by the *Lorentz force* F_L

$$F_L \equiv -e(\vec{E} + \vec{v} \times \vec{B}) \tag{2.5}$$

Quiver Energy

To gain intuition about some quantities of interest for laser-matter interactions, let's consider a simple problem of an electron of charge $-e$ governed by eq. (2.5) with a negligible magnetic field B. Additionally, only consider 1D motion in the oscillating field $E = E_0\cos(\omega t)$ for a laser field of frequency ω. Then, the equation of motion is

$$\frac{dv}{dt} = -\frac{eE_0}{m}\cos(\omega t) \tag{2.6}$$

We can integrate this equation to obtain the velocity and position as a function of time (assuming $x_0 = v_0 = 0$)

$$v(t) = -v_{\text{osc}}\sin(\omega t) \tag{2.7}$$

$$x(t) = \frac{v_{\text{osc}}}{\omega}[\cos(\omega t) - 1] \tag{2.8}$$

where $v_{\text{osc}} \equiv (eE_0)/(m\omega)$ is defined as the *quiver velocity*. From Equation 2.7, we can calculate the kinetic energy gained by an electron as $U_p \equiv \frac{1}{2}m\langle v^2\rangle = \frac{1}{4}mv_{\text{osc}}^2$ which is known as the *ponderomotive potential (energy)*. This energy represents the cycle-averaged quiver energy of an electron in an electromagnetic field. A more commonly used term is the dimensionless *normalized vector potential* a_0 which is closely related to the quiver velocity

$$a_0 \equiv v_{\text{osc}}/c = \frac{eE_0}{m\omega c} \tag{2.9}$$

Ultra-intense laser-matter interactions involve relativistic electrons which are produced when $a_0 \gtrsim 1$. In terms of the field, $a_0 \sim 1$ corresponds to a peak electric field $E_0 = \frac{2\pi mc^2}{e\lambda} \simeq 4\,\text{TV}\,\text{m}^{-1}$. In terms of the peak intensity, $I_0 = \frac{1}{2}c\epsilon_0 E_0^2 \simeq 2\times10^{18}\,\text{W}\,\text{cm}^{-2}$ for this electric field. Consequently, the threshold for relativistic interactions is commonly understood as $I_0 \gtrsim 1\times10^{18}\,\text{W}\,\text{cm}^{-2}$.

Ponderomotive Force

The above approach yields some important scales for laser-matter interactions, but only describes the interaction of a plane wave that is spatially homogeneous. A real laser field would be spatially inhomogeneous and we can express $E(x) \approx E_0 + xE_0'(x)$ to first order. This modifies the equation of motion as

$$\frac{dv}{dt} = -\frac{eE_0}{m}\cos(\omega t) - \frac{eE_0'}{m}\cos(\omega t)[\frac{v_{\text{osc}}}{\omega}(\cos(\omega t) - 1)] \tag{2.10}$$

where we've inserted the expression for x from eq. (2.8) which should be approximately true for small x. This equation can be simplified and separated into oscillating and non-oscillating components as

$$\frac{dv}{dt} = -\frac{eE_0}{m}[\cos(\omega t)(1 - \frac{E_0'v_{\text{osc}}}{e_0\omega}) + \frac{E_0'v_{\text{osc}}}{2\omega E_0}\cos(2\omega t)] - \frac{eE_0'v_{\text{osc}}}{2m\omega} \tag{2.11}$$

Over many cycles, the oscillating components will average out to zero and the remaining term is given by $\langle F_p\rangle = m\frac{dv}{dt} = -\frac{eE_0'v_{\text{osc}}}{2m\omega}$ and is called the *ponderomotive force*. We can

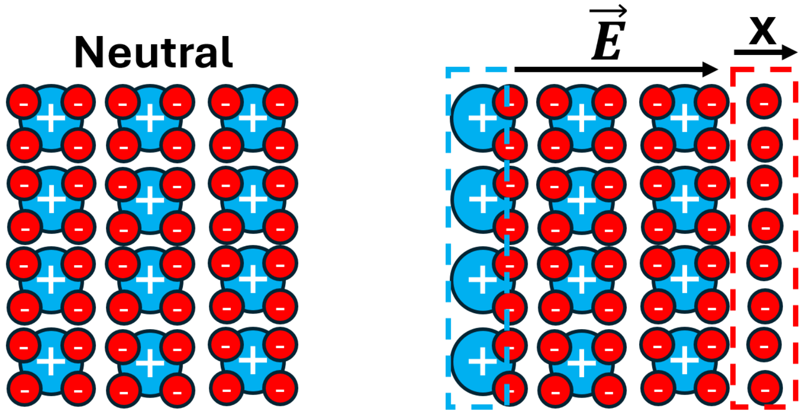

Figure 2.1: An initially charge-neutral plasma is depicted on the left. On the right, the electrons are displaced by a distance x creating a charge separation and electric field akin to a parallel-plate capacitor directed towards the right. Adapted from Smith [4].

generalize this to 3D and express this time-averaged force in several different, equivalent ways

$$\langle F_p \rangle = -\frac{e^2}{2m\omega^2}|E_0|\nabla E_0 = -\frac{mc^2}{4}\nabla(a_0^2) = -\nabla U_p \tag{2.12}$$

where

$$U_p = \frac{e^2 E_0^2}{4m\omega^2} = \frac{1}{4}mv_{\mathrm{osc}}^2 \tag{2.13}$$

is the ponderomotive potential energy introduced earlier.

The ponderomotive force is an important mechanism in the absorption of laser energy by electrons which will be expanded upon in section 2.1.4.

2.1.3 Properties of a Plasma

The quasi-neutrality condition reflects the fact that a plasma is charge neutral throughout its volume in a similar way to an ideal conductor: mobile electrons will reorganize themselves in the presence of an external electric field to maintain zero field (or constant potential). The simplest plasma description will assume the ions are immobile (due to being much heavier than the electrons) and can be treated as a constant neutralizing background density n_i for the electrons of density $n_{e,0} = Zn_i$ (for a plasma with atomic number Z).

Plasma Electron Oscillations

A simple example can be illustrated by fig. 2.1 which shows a sheet of negative charge density $-\sigma = -en_e x$ displaced to the right a small distance x. The region in the bulk of the plasma will experience a force from the parallel plate "capacitor" fields directed to the left.

$$F = m\frac{d^2x}{dt^2} = -e\frac{en_e x}{\epsilon_0} \tag{2.14}$$

which has the form of a restoring force that brings the charge imbalance back to the center of the plasma. This oscillatory motion has an associated frequency

$$\omega_{p,e} = \sqrt{\frac{n_e e^2}{m_e \epsilon_0}} \tag{2.15}$$

that gives the timescale for electron motion in the plasma. This characteristic frequency shows why plasmas support collective motion (in opposition to a neutral gas in which collisions between individual particles only happen). To get a feeling for this timescale, let's assume a somewhat typical electron density $1 \times 10^{29}\,\mathrm{m}^{-3}$ in laser-plasma interactions to yield a timescale of $\omega_{p,e}^{-1} \simeq 0.1\,\mathrm{fs}$.

Naturally (without externally imposed forces), these fluctuations in charge would be caused by thermal motions of electrons with a characteristic speed v_{th}

$$v_{th} = \sqrt{\frac{k_B T_e}{m}} \tag{2.16}$$

Due to the strong restoring force from the charge separation, the electrons can only move a short distance λ_D, called the Debye length, out of equilibrium in this timescale. We can estimate this length by equating $v_{th} = \lambda_D/t \simeq \lambda_D \omega_{p,e}$ and solve for λ_D.

$$\lambda_D = \frac{v_{th}}{\omega_{p,e}} = \sqrt{\frac{\epsilon_0 k_B T_e}{n_e e^2}} \tag{2.17}$$

Physically, λ_D gives a length scale over which the electrostatic force persists in a plasma. Within a distance λ_D from some perturbation, charges will feel a force, and outside this distance, the charges will be completely shielded like that of an ideal conductor.

Fluid Model

This description of a plasma as a sea of electrons with collective motion that allows wave-like motions naturally lends itself toward a fluid model. The first component of this model stems from eq. (2.5) whose explicit time and space dependence can be expressed through $\frac{dp}{dt} = m(\frac{\partial v}{\partial x}\frac{\partial x}{\partial t} + \frac{\partial v}{\partial t}) = m(\frac{\partial v}{\partial t} + v\frac{\partial v}{\partial x})$ (just considering one spatial dimension for simplicity). The second component of this model is the effect of the pressure gradient from thermal motions. Particles will tend to migrate from areas of higher pressure to lower pressure, where the thermal pressure is typically given by the familiar ideal gas law equation of state $p = n_e k_B T_e$. Consequently, the equation of motion should have a term that is opposite to the pressure gradient direction (i.e. $-\nabla p$). Combining these two components together in a generalized 3D equation results in

$$mn_e(\frac{\partial \vec{u}}{\partial t} + (\vec{u} \cdot \nabla)\vec{u}) = -en_e(\vec{E} + \vec{u} \times \vec{B}) - \nabla p \tag{2.18}$$

where we've changed the single particle velocity $\vec{v}$ to the fluid velocity $\vec{u}$ and multiplied by the electron density n_e to ensure correct units with the pressure gradient term. Then, let's look for a simple radially symmetric solution where the fluid velocity $u = 0$, magnetic field B is negligible, and the temperature is constant (isothermal). Then,

$$n_e eE = -k_B T_e \frac{\partial n_e}{\partial r} \tag{2.19}$$

and by relating the electric field to the potential $E = -\frac{dV}{dx}$, this equation can be integrated from $n_{e,0} \to n_e$ and $0 \to \phi$ to obtain

$$n_e = n_{e,0} \exp(\frac{e\phi}{k_B T_e}) \tag{2.20}$$

which is referred to as the *Boltzmann relation* for electrons [30]. We can get an approximate solution to this equation when the potential ϕ is only slightly larger than the equilibrium $\phi = 0$, which can be found when $e\phi << k_B T_e$. We can Taylor expand the density to obtain

$$n_e \approx n_{e,0}(1 + \frac{e\phi}{k_B T_e}) \tag{2.21}$$

and if we assume a fully ionized plasma with immobile ions of charge Z, the density of ions satisfies $ne, 0 = Zn_i$ and eq. (2.4) becomes

$$\epsilon_0 \nabla^2 \phi = -en_{e,0} + en_e = en_{e,0}[1 + \frac{e\phi}{k_B T_e} - 1] = \frac{e^2 n_{e,0}\phi}{k_B T_e} \tag{2.22}$$

This equation admits solutions of an exponentially decaying potential

$$\phi(r) = \frac{Q}{r} \exp(-\frac{r}{\lambda_D}) \tag{2.23}$$

where $\lambda_D = \sqrt{\frac{\epsilon_0 k_B T_e}{n_{e,0} e^2}}$ is the Debye length from eq. (2.17). A visualization of the decaying potential from eq. (2.23) is shown in fig. 2.2. Looking at the center panel, we can see the fields drop off quickly within a distance λ_D in contrast to the left panel's potential that extends much further out in distance r. The exponentially decaying potential is a feature of plasmas and highlights the ability of plasma electrons to shield fields in a distance λ_D.

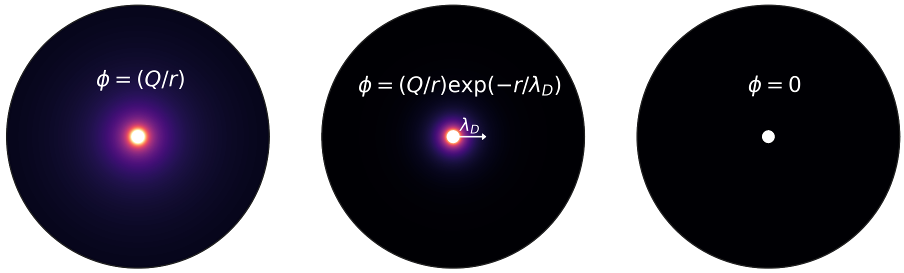

Figure 2.2: Visualization of the electric potential as a function of radial distance away from a positive point charge at the origin in three scenarios: vacuum (left), plasma (center), ideal conductor (right). Brighter colors show a higher value of ϕ. In the center panel, the debye length λ_D is shown.

Plasma Conditions

Putting all this together, we can define several conditions that must be satisfied for a plasma [30]. Quasi-neutrality dictates that the plasma should be largely charge neutral. The only regions that aren't charge neutral are those that fall within λ_D of some charge imbalance. Therefore, if L is the length scale of the system in which the plasma resides, we require that $\lambda_D \ll L$. However, this condition is not sufficient because an ideal conductor has $\lambda_D = 0$ but is not a plasma due to the absence of collective behavior. Collective behavior can be enforced by asserting that there are enough electrons N_D within a spherical volume of radius λ_D. The corresponding equation is $N_D = n_e(\frac{4}{3}\pi\lambda_D^3) \gg 1$. The final condition is that electrostatic interactions should dominate over collisions because the collective behavior (e.g. plasma oscillations) originates from the electrostatic forces. This means that the period of oscillations ($\omega_{p,e}^{-1}$) should be less than the mean time between collisions.

2.1.4 Absorption of Energy

In order for a laser to couple energy to the plasma electrons, some absorption mechanism needs to take place. The most obvious way that electrons can gain energy is through collisions with other energetic electrons and ions. However, the collision frequency is known to get smaller as the temperature goes up [9], so much so that plasmas can be treated as collisionless for ultra-intense laser experiments. Below, some of the most common known heating mechanisms are summarized.

Critical Density

First, we will look at how the electric field from an oscillating electric field penetrates a plasma. Using eqs. (3.2) and (3.4) combined with the vector identity $\nabla \times (\nabla \times \vec{E}) = \nabla(\nabla \cdot \vec{E}) - \nabla^2 \vec{E}$ [31], we can solve for the vector wave equation in terms of only $\vec{E}$.

$$(\nabla^2 - \frac{1}{c^2}\frac{\partial^2}{\partial t^2})\vec{E} = \mu_0 \frac{\partial J}{\partial t} + \nabla(\nabla \cdot \vec{E}) \tag{2.24}$$

We can look for solutions of $\vec{E} = E(x)\cos(\omega t)\hat{x}$ that vary spatially only in the x direction. We are assuming $E(0)$ is the amplitude of the electric field at the boundary between vacuum $x < 0$ and matter $x > 0$ and wish to understand the form of $E(x)$ when $x > 0$. To proceed, we can assume the current density can be related to the drift velocity [32] by $J = -n_e e u$ where u is the electron fluid velocity that satisfies eq. (2.18). Ignoring B and thermal pressure, this relationship becomes

$$\frac{\partial \vec{J}}{\partial t} = \frac{n_e e^2}{m} E = \omega_p^2 \epsilon_0 \vec{E} \tag{2.25}$$

using eq. (2.15) which can be combined with eq. (2.24) to obtain a differential equation for the electric field

$$[\nabla^2 + \frac{\omega^2}{c^2}(1 - \frac{\omega_p^2}{\omega^2})]\vec{E} = 0 \tag{2.26}$$

By just focusing on the x-dependence, we can simplify this equation to

$$\frac{d^2 E}{dx^2} = \frac{1}{l_s^2} E \tag{2.27}$$

where $l_s^2 \equiv \frac{c^2}{\omega^2 - \omega_p^2}$ defines the *skin depth* l_s. In the case where $\omega < \omega_p$, l_s^2 is negative and the solution has a sinusoidal dependence

$$E(x) = E(0)\cos(x/l_s) \tag{2.28}$$

On the other hand, when $\omega > \omega_p$, l_s^2 is positive and the solution has an exponential dependence

$$E(x) = E(0)\exp(-x/l_s) \tag{2.29}$$

This "evanescent" behavior when $\omega > \omega_p$ occurs because the electrons cannot respond fast enough to the higher frequency ω. Since the field cannot propagate effectively for $x > 0$, the plasma ends up reflecting a significant portion of the light. Since wavelength (and frequency) is fixed from the laser, we can reformulate this finding in terms of electron density. The critical density n_c is defined as the electron density where $\omega = \omega_{p,e}$. Using eq. (2.15), this can be expressed as

$$n_c \equiv \frac{m\epsilon_0}{e^2}\omega^2 \tag{2.30}$$

When $n_e > n_c$, the plasma is said to be *overdense* and most of the laser light gets reflected. When $n_e < n_c$, the plasma is said to be *underdense*, and the laser light can propagate through the plasma.

A typical Ti:Sapphire laser has a wavelength of 0.8 µm which corresponds to a critical density of $n_c \simeq 1.7 \times 10^{27}\,\mathrm{m}^{-3}$. In this work, two materials are of interest: gold and ethylene glycol which have densities of $19.3\,\mathrm{g\,cm}^{-3}$ and $1.11\,\mathrm{g\,cm}^{-3}$ respectively. These mass densities correspond to a number density of electrons $5.9 \times 10^{28}\,\mathrm{m}^{-3}$ and $1.1 \times 10^{28}\,\mathrm{m}^{-3}$ respectively assuming a singly ionized plasma. If the plasmas were multiply ionized, these densities would be even higher. Even though these "solid density" plasmas are clearly overdense, experiments show energy is able to efficiently couple to the electrons. Consequently, there must exist mechanisms of absorption that are consistent with the fact that most of the laser energy can only be deposited in a small depth l_s into the plasma.

Resonance Absorption

The previous discussion applied to an electric field directed in the x-direction. For gaussian laser beams, the electric field is always perpendicular to the direction of propagation. So, if the laser beam is to be directed toward a target at $x = 0$, normal incidence would imply that the electric field $E_x = 0$. Additionally, an s-polarized beam would have an electric field only in the z direction. As a result, the typical model of a laser beam depositing energy into a plasma involves a p-polarized laser beam traveling obliquely in the $x-y$ plane with some angle of incidence θ_i measured with respect to the normal direction of the target. Physically, plasma oscillations occur through fluctuations in density which are going to be the strongest in the x direction due to the interface between vacuum and matter.

Furthermore, Kruer [33] argues that the reflection of light at oblique incidence occurs at a density $n_e = n_c \cos^2(\theta_i)$ by enforcing momentum conservation of the electric field component in the y direction. Even though we've discussed density profile as an abrupt step: from 0 to n_e from crossing $x = 0$, an actual experiment would see some pre-heating of the target before the target becomes ionized and behaves as a mirror at the critical density. This can be characterized by some scale length $L_p \equiv n_e(\frac{\partial n_e}{\partial x})^{-1}$ which is smaller for steeper density profiles. As a result, at higher incidence angles, the evanescent portion of the electric field has to travel further into the underdense region of the target to reach the critical density.

When the frequency of the laser $\omega \simeq \omega_p$, the laser light is in resonance with the plasma oscillations and the energy can be most efficiently absorbed. To maximize the amount of

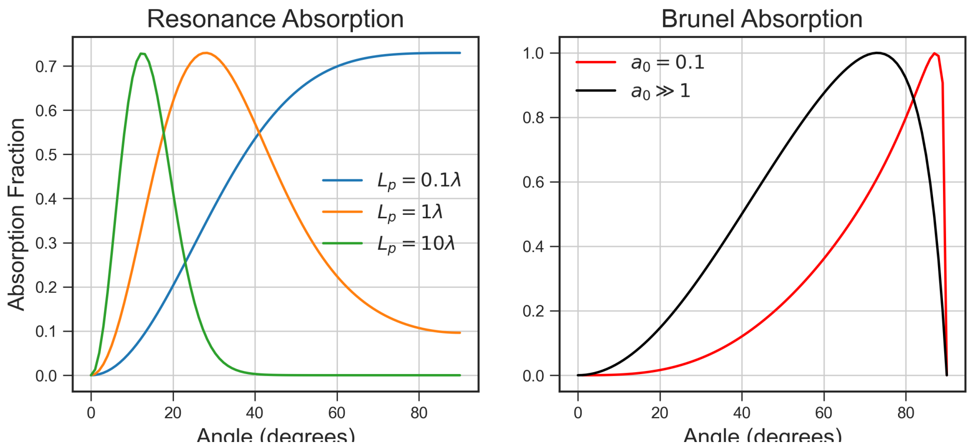

Figure 2.3: Absorption fraction as a function of incidence angle θ_i. For resonance absorption, the density scale length L_p is varied in terms of the laser wavelength $\lambda = 0.8\,\mu$m. For the Brunel mechanism, fractions are plotted for two regimes $a_0 \ll 1$ (where a value of $a_0 = 0.1$ was chosen) and for $a_0 \gg 1$ (which has no dependence on a_0).

energy reaching the critical density surface in resonance, we would want θ_i to be large so that the electric field has a significant component in the x direction, but also small enough so that the field doesn't diminish too much by traveling in the evanescent underdense region. Denisov [34] and others [35–37] addresses this question and develops a model for this so-called *resonance absorption* An approximate version of this formula is given by Kruer [33]

$$\phi(\tau) \simeq 2.3\tau \exp(-2\tau^3/3) \tag{2.31}$$

where $\tau \equiv (kL_p)^{1/3} \sin(\theta_i)$ takes into account both the scale length and incidence angle. fig. 2.3 shows the fractional absorption $\phi(\tau)^2/2$ of the incident light from this model as a function of θ_i for various scale lengths.There is an optimal angle $\theta_{max} \approx \arcsin(0.8(kL_p)^{-1/3})$ that maximizes the absorption fraction (although Kruer notes that his simple model overestimates the peak absorption – the fraction should peak at around 0.5 [33]).

Brunel Heating

Resonance absorption only makes sense when the amplitude of the plasma oscillations $x_{\text{osc}} = v_{\text{osc}}/\omega = \frac{a_0\lambda}{2\pi}$ is less than the scale length L_p [9], otherwise there is not enough available space for the oscillations to take place. For $\lambda = 0.8\,\mu$m and $a_0 = 1$, $x_{\text{osc}} = 127\,$nm. However, for extremely small scale-lengths, efficient electron heating can still be observed [38]. Consequently, a different type of heating mechanism is responsible in this case (somewhat confusingly) called "not so resonant, resonant absorption" [8]. This model, developed by Brunel, is also known as *vacuum heating* and will be explained below.

Before explaining the Brunel mechanism, I should the basics of the 3-step model used for high-harmonic generation [39]. Readers may find this model more familiar due to the recent 2023 Nobel Physics Prize won by Ohio State's Pierre Agostini [40] which utilized the ideas of this model to produce attosecond pulses. This model involves a strong oscillating electric field $E(x) = E_0 \cos(\omega t)$ incident on an atom. Now, assume an electron is ionized at $t = t^*$. Under the influence of the oscillating field, the (initially stationary) electron will gain and lose energy by moving away from the atom and returning back toward the atom. When $t^* \neq n\pi$ for integer n, it is actually possible for the electron to return back to the atom with non-zero energy. In fact, when $\omega t^* \approx 17^\circ + n(180^\circ)$, the electron returns with an energy peaking at $3.17U_p$ where U_p is the ponderomotive potential given by eq. (2.13). Furthermore, modeling the ionization rate through quantum-mechanical tunneling of an electron through a Coulomb potential warped by the oscillating laser field, we also determine that the most probable energy for an electron is strongly peaked at the $3.17U_p$ cutoff. In short, this model shows how a laser field can produce electrons with energy on the scale of the ponderomotive potential with high probability at a frequency of twice per optical cycle.

In the Brunel mechanism [8], we are considering a laser field incident on a planar target at $x > 0$ and vacuum at $x < 0$. In order for the electrons to escape the target, there needs to be some component of the electric field in the x direction. Thus, we need to consider oblique incidence and p-polarization just like with resonance absorption. When the plasma scale length is small, the electrons will be able to travel far enough in the $x < 0$ to escape the plasma entirely and gain energy on the order of U_p in a similar fashion to Corkum's model [39]. Electrons arriving back to the target at just the right time will penetrate deeper than the skin depth $l_s \approx c/\omega_p$ and be inaccessible to the laser field [9]. These *hot electrons*, generated primarily on the front surface of the target, will provide the energy to heat the remainder of the overdense region of the target that the laser field cannot directly access.

As mentioned, the optimal angle would appear to be for grazing incidence ($\theta_i = 90^\circ$), but Gibbon notes that accounting for imperfect reflection of the laser field and relativistic energies of the electrons, the efficiency no longer diverges at $\theta = 90^\circ$ [9]. In fig. 2.3, some estimates for the absorption efficiency are plotted according to a simplified model developed by Gibbon [9] based on Brunel [8].

Other Mechanisms

When the laser field penetrates a distance $l_s \approx c/\omega_p$ into the overdense region of the target, the electrons can heat up through collisions at an absorption rate $\eta \propto \frac{\nu_{ei}}{\omega_{p,i}}$ [9] where ν_{ei} is the electron-ion collision frequency. This type of absorption is called the *skin effect*. In this case, we see Fresnel-like reflection and absorption (see [41]) that is effective for large incidence angles. Even when the collision frequency is low, we can still get efficient absorption as long as the thermal electron motions are large compared to the skin depth (i.e. $v_{th}/\omega > l_s$)

[9]. This phenomena is called the *anomalous skin effect* that is also most effective at large incidence angles.

All of the mentioned phenomena work best at oblique incidence in p-polarization. But, for relativistic intensities, additional heating mechanisms arise. When $a_0 \gtrapprox 1$, the magnetic portion of eq. (2.5) becomes significant. At normal incidence, the electric and magnetic field components both fall in the $y-z$ plane. The electric fields move the electrons strongly causing a current $\vec{J}$ which in turn will interact with the laser magnetic field $\vec{B}$ in the direction perpendicular to both. As a result, this type of heating is known as $\vec{J} \times \vec{B}$ heating [9, 42]. Because $\vec{J} \times \vec{B}$ is in the direction of propagation, this effect is most pronounced at normal incidence. (CAN Maybe talk about how circular polarization mitigates JxB heating)

At even higher intensities, the laser can directly impart energy to the electrons through radiation pressure [43] because photons themselves carry momentum. These mechanisms are explored further in section 2.2. In reality, all experiments involve a combination of several different electron heating mechanisms. Consequently, many experiments and simulations have been devoted to parametric studies that show how parameters (L_p, θ_i, polarization, a_0, etc.) affect electron absorption (CITATIONs needed)

2.2 Ion Acceleration

The previous section gave an overview of the laser-plasma interactions and how they can efficiently couple energy into hot electrons. Regardless of heating mechanism, one theme is common to all – the energy gained by an electron's quiver motion in an oscillatory field, known as the ponderomotive potential (eq. (2.13)) sets the scale for the hot electron temperature T_h. That equation was only valid for non-relativistic electrons, so we must replace $U_p = \frac{1}{4} m v_{\text{osc}}^2$ with the relativistic kinetic energy $U_p \equiv (\gamma - 1)mc^2$ where $\gamma = 1/\sqrt{1 - \frac{v_{\text{osc}}^2}{c^2}}$ defines the lorentz factor. We can combine this with the relativistic momentum $p = \gamma m v_{\text{osc}}$ and eq. (2.9) to determine an approximate expression of γ in terms of a_0

$$\gamma \simeq \sqrt{1 + a_0^2} = \sqrt{1 + \frac{I_{18}\lambda_{\mu m}^2}{1.37}} \tag{2.32}$$

where I_{18} is the peak intensity of the laser pulse in 1×10^{18} W cm^{-2} and $\lambda_{\mu m}$ is the wavelength in μm. In 1992, Wilks [5] conducted simulations to show that T_h is on the order of U_p.

$$k_B T_h = mc^2(\gamma - 1) \tag{2.33}$$

In fig. 2.4, we can see that the *Wilks scaling* (pink) closely matches ultra-intense laser experiments. The other scalings in the figure are similarly validated by computational simulations and are all proportional to $(I\lambda^2)^\alpha$, where $0 < \alpha \leq 1$. As a result, the product $I\lambda^2$ is an important quantity in laser-plasma experiments and is called the *irradiance*. Wilks

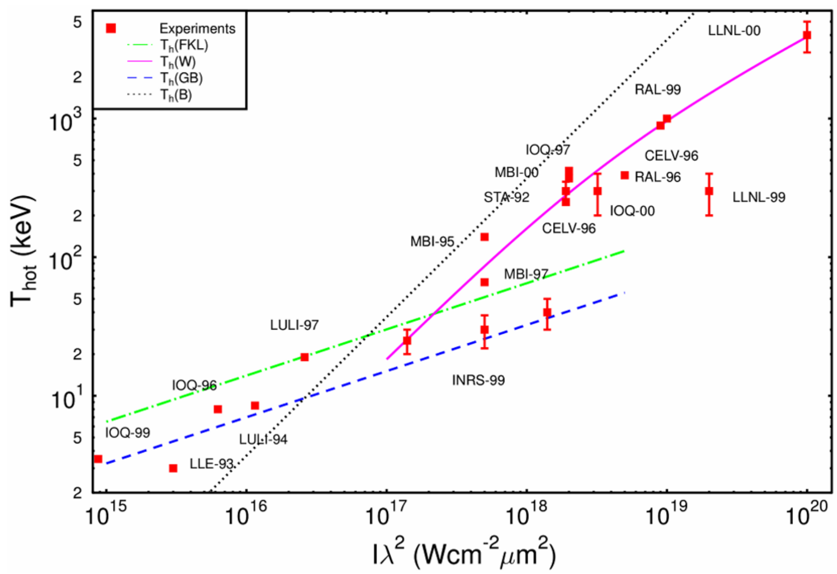

Figure 2.4: Experimentally recorded hot electron temperatures as a function of irradiance $I\lambda^2$ are plotted as red squares. The empirical scaling models are given by Wilks [5](pink, solid), Gibbon and Bell [6](blue, ashed), Forslund et. al. [7](green, dash-dot), and Brunel [8](black, dotted). Figure is taken from Gibbon [9]

also outlines a way to measure the hot electron temperature in his simulations [5] by taking the slope of $\frac{dN_e}{dE}$ in the MeV regime and is something I do in (MAYBE REFERENCE FIGURE FROM CH4 of HOT ELECTRON SPECTRA)

Since protons are 1836 times as massive as electrons, they are much harder to accelerate and on the scale of femtosecond pulse interactions, they are essentially immobile. Despite this, ultra-intense laser experiments have demonstrated proton acceleration is possible. This section will explain the TNSA mechanism for accelerating protons and light ions which is heavily dependent on T_h. Then, we will discuss alternative acceleration mechanisms. Finally, we'll overview some important applications.

2.2.1 Target Normal Sheath Acceleration

The observation of energetic protons off the rear side of thin plastic and gold targets has been documented throughout a variety of experiments since the 80s [44]. It might sound unintuitive that we would even see protons in the first place; after all, when shooting a target like aluminum, one would expect aluminum ions. It turns out that there is always an important and measurable surface contamination layer, primarily composed of hydrogen and light hydrocarbons [45]. Allen [46] showed that when removing the surface contaminant from the backside, we see a strong suppression in ion acceleration. This points to the contaminant layer being the crux of what is accelerated.

TNSA Models

Expansion models have been long known since the 70s and 80s (e.g. Crowe [47] and Kishimoto [48]) that describe the acceleration of protons with experiments (e.g. Tan [44]) as well. However, the advent of Chirped Pulse Amplification [49] in 1985 by Donna Strickland and Gerard Mourou allowed the intensities of the laser light to increase to relativistic levels ($a_0 > 1$) with sub-ps pulse durations. This technology dramatically impacted the field of laser-plasma interactions because it allowed new relativistic regimes of ion acceleration to be explored – for this work they won the Nobel Prize [50].

The field of ultra-intense proton acceleration kicked off in the year of 2000 with a group at Michigan [51] finding 1.6 MeV protons from a thin aluminum foil with a $3 \times 10^{18}\,\mathrm{W\,cm^{-2}}$ class laser at normal incidence. Then, Rutherford Appleton Laboratory found 30 MeV protons [52] from a $5 \times 10^{19}\,\mathrm{W\,cm^{-2}}$ class laser incident on a lead target at 45° incidence. Shortly after, Lawrence Livermore National Laboratory (LLNL) found energies up to 58MeV [53] from a $3 \times 10^{20}\,\mathrm{W\,cm^{-2}}$ class laser on a gold target at 45° incidence.

Now that efficient MeV proton acceleration had been achieved through multiple studies, a more thorough comprehensive picture of the physical process was desired. In 2001, Wilks [54] summarized much of the existing literature including the isothermal expansion model [47], existence of a maximum cutoff energy [48], and dependence on hot temperature [5]. Then, he described the TNSA process in the following way [54]

> ... the prepulse creates large plasma in front of a solid target. Once the main pulse hits the target, a cloud of energetic electrons (1-10 MeV in effective temperature) is generated, which extends past the ions on both the front and back of the target. Since the protons on the back are in a sharp, flat density gradient, they are accelerated quickly (in the first few μm off the target) to high energies in the forward direction ... On the front, the outermost ions are in a sphere, in a long scale length plasma (due to prepulse) and therefore are accelerated to lower energies, and are spread out into 2π steradians.

A visual of the TNSA process can be seen in fig. 2.5. Although Wilks [54] provided a physical picture of the TNSA process, existing models didn't always match up to experiments. For this reason, the ensuing decade saw much progress in the development of models to describe the spectrum of TNSA accelerated protons. Perego [55] gives a good review of some of the leading models developed and tested against experiments in the 2000s and these models will be summarized below.

First, are the isothermal expansion (fluid) models which include Mora's "Plasma Expansion into a Vacuum" [16] (2003) that combine eqs. (2.4) and (2.20) with fluid eqs. (5.6a) and (5.6b). This model underlies the work done in chapter 5, where it is explained in more

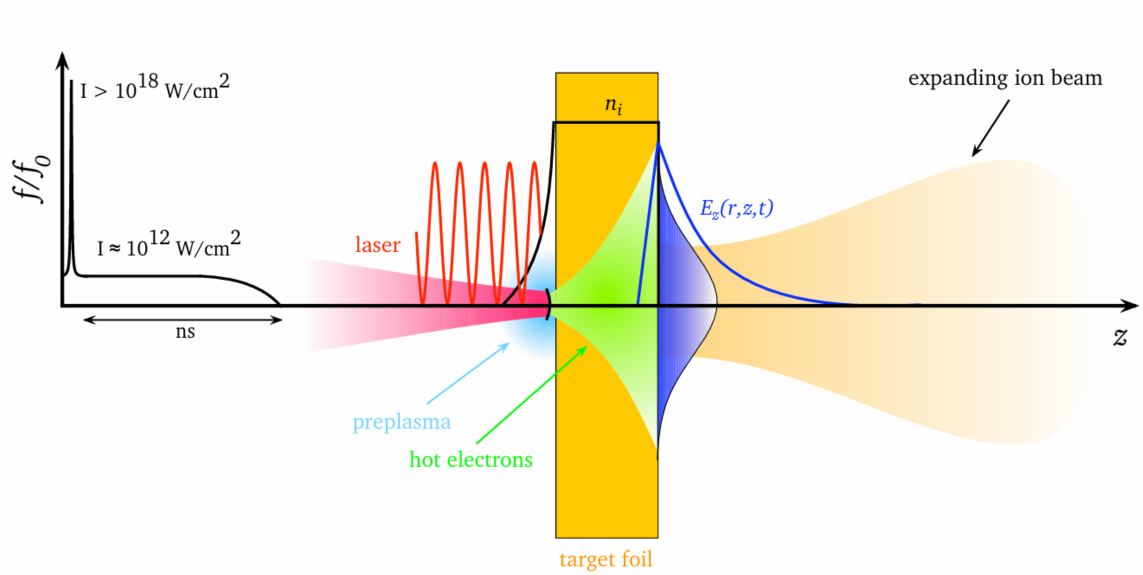

Figure 2.5: The TNSA process is depicted. First, an intense laser pulse irradiates the front side of a target foil of few μm thickness. This generates hot electrons that stream through the foil and re-emerge in a cloud on the rear side. The charge separation of the hot electrons and positively charged target creates intense longitudinal fields ($\sim$ TV/m) that accelerate light ions in the mostly target normal direction. This figure was taken from Roth [10]

detail, and has the issue of predicting proton energies that can go up to arbitrarily high values. As a remedy, Mora introduces a finite acceleration time τ which is of the order of the pulse duration. Mora [56] addresses this in a different way (2005) by instead assuming an adiabatic model and limiting the target to be a thin foil (instead of a semi-infinite target).

Alternatively, Passoni and Lontano [57] introduces an upper limit to the integration range of the electric potential instead of using the fluid equations. In this approach, the electrostatic fields determined from the potential are considered static, and the ensuing ion dynamics is determined by placing a test ion in the field. Further iterations incorporate some distribution of speeds for the electrons (non-relativistic Maxwell-Boltzmann [58] or relativistic Maxwell-Juttner [59]) and use an empirically determined scaling for the peak energy of electrons (as a function of laser energy) that do not escape the system [60].

Furthermore, some hybrid models include elements of both fluid and quasistatic models like Robinson [61] and Albright [62].

Optimization of TNSA process

Since the TNSA process is intimately related to the hot electron process at the front of the target and the flat density gradient at the back, many efforts have been taken to design targets that optimize ion acceleration. Patel [63] used spherically shaped targets to act as a lens that can focused the proton beam. MacKinnon [64] showed lower target thickness leads to higher proton energy due to a higher mean density of hot electrons at the surface. More recent experiments have even used nanowires [65] and microtubes [66]. Many experiments generally find that there is an optimal level of pre-expansion of the target that enhances hot electron generation and ion acceleration (e.g. McKenna [67]).

Another way to increase the peak proton energy of the emitted spectrum is to use two spatially aligned pulses. If one pulse has a delay with respect to the other, the first pulse could pre-expand the target to provide an optimal electron density at the front surface [68]. If the pulses are also temporally aligned, the constructive interfere at the target front surface may prove beneficial [14]. The second approach is called enhanced target normal sheath acceleration (eTNSA) and chapter 4 is devoted to this phenomenon.

See the review article by Roth [10] for a more comprehensive list of the different approaches to enhance TNSA.

2.2.2 Other Acceleration Mechanisms

TNSA is not the only method in which protons can be accelerated. For intensities of greater than 10^{21} W cm^{-2}, laser-induced ion shocks can start to play a significant role [69]. For even higher intensities $\sim 10^{23}$ W cm^{-2}, the radiation pressure of the electromagnetic wave can efficiently transfer momentum to the ions [69]. See Macchi [43] for a more in depth discussion on these topics. One way to differentiate the TNSA regime from other regimes is through the following equation relating a_0 to various properties of the laser and target

$$a_0 = n_e \lambda r_e l_0 = 224 \left(\frac{n_e}{1 \times 10^{29}\,\mathrm{m}^{-3}} \right) \left(\frac{l_0}{1\,\mu\mathrm{m}} \right) \tag{2.34}$$

Lezhnin [11] uses this equation to differentiate TNSA from two other mechanisms: radiation pressure acceleration (RPA) and Coulomb Explosions; this can be seen in fig. 2.6. If the laser intensity is sufficiently high and density is low enough to be transparent, the laser can quickly sweep away most electrons to leave behind a strongly positive target. The repelling coulomb force will cause the protons to expand outwards in all directions.

When the radiation pressure $P_{\mathrm{rad}} \approx 2I_0/c$ is significant enough to overcome the thermal expanding pressure $n_e k_B T_e$, ions can accelerate directly through the transfer of momentum. [43]. In this regime, laser absorption into hot electrons by traditional mechanisms would be detrimental. By shooting the laser at normal incidence with circular polarization, resonance absorption and $\vec{J} \times \vec{B}$ heating can be minimized as seen in section 2.1.4.

For thick targets, this immense pressure can impart a parabolic deformation that allows the laser to penetrate further. This is the regime of *hole boring*. Targets thin enough where the hole boring process reaches the target rear in a time less than the pulse duration are in the *light sail* regime. [43].

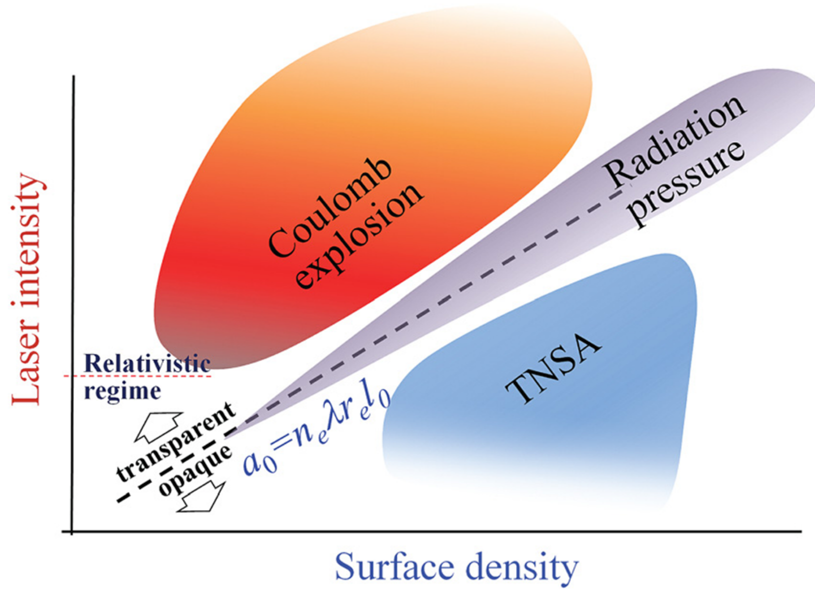

Figure 2.6: The regimes of various three different acceleration mechanisms are displayed in terms eq. (2.34). This figure was taken from Roth [11]

Wakefield Acceleration

All the aformentioned acceleration processes only make sense for overdense targets whose electron density is greater than the critical density ($n_e > n_c$). This is because the critical density surface is the primary area where the laser deposits energy into hot electrons. If the target plasma has $n_e < n_c$, the target is said to be underdense and there is no critical density surface where the laser interacts with. Tajima and Dawson [70] first proposed the idea of a "Laser Electron Accelerator" in 1979 that is capable of accelerating electrons to high energies through the non-linear ponderomotive force. If the conditions are just right, the electrons can "surf" a plasma wave in the wake of the pulse and pull along positive ions in a process now known as laser wakefield acceleration (LWFA). A comprehensive review of the subject can be found here [71].

Chapter 3
Computational Methods

3.1 The Particle-In-Cell Method

The PIC method involves solving Maxwell's Equations on a grid

$$\nabla \cdot \vec{E} = \frac{\rho}{\epsilon_0} \tag{3.1}$$

$$\nabla \times \vec{E} = -\frac{\partial \vec{B}}{\partial t} \tag{3.2}$$

$$\nabla \cdot \vec{B} = 0 \tag{3.3}$$

$$\nabla \times \vec{B} = \mu_0(\vec{J} + \epsilon_0 \frac{\partial \vec{E}}{\partial t}) \tag{3.4}$$

This is combined with the lorentz force

$$\vec{F} = q(\vec{E} + \vec{v} \times \vec{B}) \tag{3.5}$$

which determines the motions (i.e. $\vec{r}$ and $\vec{v}$) of charged particles by integration. It is impossible to keep track of the true numbers of particles in this type of simulation which would be roughly on the order of Avogadro's number $\sim 10^{23}$. Instead, we lump many particles together into what is called a *macro particle*. For example, one "macro electron" could contain 1 trillion "real electrons". Also, we cannot hope to have infinite precision in calculating quantities of interest. Spatially, we must separate the simulation volume into a grid where each cell has length Δx, Δy, and Δz in the x, y, and z direction respectively. Temporally, we introduce a time step Δt which allows us to propagate Maxwell's Equations forward in time by Δt for every iteration.

For simplicity, non-relativistic equations will be introduced in this section, but they can easily be generalized to the relativistic versions which are implemented in modern PIC codes. Additionally, some of the equations will assume a 2D grid, but a 3D grid is similarly straightforward to generalize.

3.1.1 Densities and Shape Factors

When a simulation is initialized, all the particles will have a defined position and velocity. The charge density $\rho_{i,j}$ (for the cell at the i^{th} and j^{th} grid point in the x and y directions) is easy to compute – it is simply the sum of all the charges q_α closest to grid point (i, j) divided by the cell area: $\rho_{i,j} \equiv \frac{\sum_\alpha q_\alpha}{\Delta x \Delta y}$ (in 2D symmetry we additionally divide by 1 meter in the z direction to get the units right). The current density $\vec{J}_{i,j}$ can be obtained similarly – $\vec{J}_{i,j} \equiv \frac{\sum_\alpha q_\alpha \vec{v}_\alpha}{\Delta x \Delta y}$. Assigning the densities to the nearest grid point in this manner is sensibly called nearest grid point (NGP) by Birdsall and Langdon [72].

Since the PIC approach contains many real particles in each macro particle, it is desired to smooth the macro particle densities throughout the cell(s). We can modify the individual density contributions of particles by a shape factor $S(\vec{r_\alpha} - \vec{r})$ that depends on a particle's location $\vec{r_\alpha}$ in relation to a grid point located at $\vec{r}$. This shape factor is normalized so that integrating it over the area of the simulation yields 1 to ensure the particle number is properly being conserved. The simplest improvement over NGP would be the *top hat* shape factor (also called Cloud in Cell [72]) which assigns density contributions proportional to proximity of the nearest cells within (Δx,Δy). This has the shape of a uniform distribution and thus looks like a "top hat" in 1D. It is a 0^{th} order shape factor and can be represented by the following equation

$$S_0(x) \equiv \begin{cases} 1 & \text{if } |x| \leq 0.5\Delta x \\ 0 & \text{otherwise} \end{cases} \tag{3.6}$$

A further improvement will weigh the particles closer to a particular grid point higher than a particle further away. If this weighting is linear over an area ($2\Delta x$, $2\Delta y$), it is called the *triangle* shape factor and reprsented by the following equation in 1D

$$S_1(x) \equiv \begin{cases} 1 - \frac{|x|}{\Delta x} & \text{if } |x| \leq \Delta x \\ 0 & \text{otherwise} \end{cases} \tag{3.7}$$

It turns out that the higher order shape factors $S_n(x)$ can be represented by convolutions of $S_0(x)$

$$S_n(x) \equiv \int_{-\infty}^{\infty} S_{n-1}(x') S_0(x - x') dx' \tag{3.8}$$

and the shape factors for $n \geq 2$ are commonly called n-splines. The third order spline is used in this work and weights particles over an area ($4\Delta x$, $4\Delta y$) and is represented in 1D by

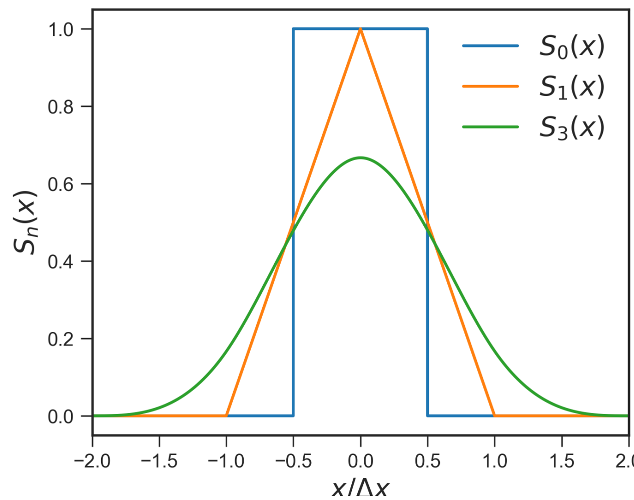

Figure 3.1: The top hat ($S_0(x)$), triangle ($S_1(x)$) and 3$^{\text{rd}}$ order spline ($S_3(x)$) are plotted in 1D.

$$b_3(x) = \begin{cases} \frac{1}{6}(8 - 12|\tilde{x}| + 6\tilde{x}^2 - \tilde{x}^3) & \text{if } 1 \leq |\tilde{x}| \leq 2 \\ \frac{1}{6}(4 - 6\tilde{x}^2 + 3\tilde{x}^3) & \text{if } |\tilde{x}| \leq 1 \\ 0 & \text{otherwise} \end{cases} \tag{3.9}$$

where $\tilde{x} \equiv x/\Delta x$ normalizes the position x. See fig. 3.1 for a comparison of the three shape factors.

These shape factors not only apply to the calculation of densities, but also to the electric and magnetic fields. In this way, the fields used to update particle positions and velocities are averaged over neighboring cells.

3.1.2 Field Solver and Particle Push

The PIC method is able to make efficient use of the second order accurate central difference approximation to compute derivatives. A simpler method like Euler integration is only first order accurate and will suffer in terms of accuracy. Higher order methods like 4th order Runge-Kutta have much higher computational costs in terms of operations per time step and memory consumption. The central difference scheme is accomplished by alternately calculating electric and magnetic fields, staggered by half a time step, in an approach called *leapfrog integration* [72]. This can be seen in the right half of fig. 3.2 where the calculations of E and J, B alternate in a "leapfrog" fashion. It turns out that this staggering also comes with some nice properties like automatically satisfying eq. (3.3). By rearranging eq. (3.2),

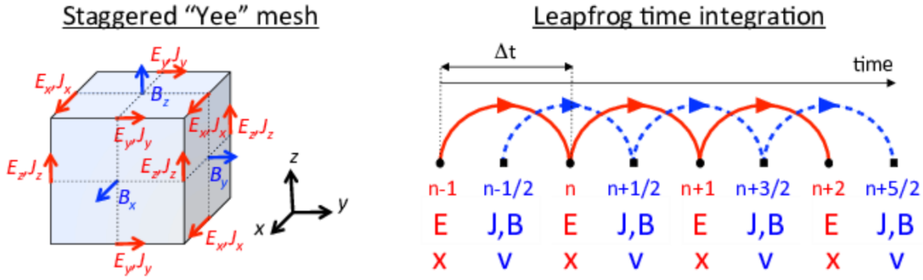

Figure 3.2: The "Yee" grid is depicted (left) where the electric and magnetic field components are staggered by half a cell. The fields, currents, position, and velocity make use of the staggered grid by leapfrog time integration (right). This picture was taken from the WarpX documentation

we can update the electric and magnetic fields through the following equations [73]

$$\vec{E}^{n+1} = \vec{E}^{n} + \Delta t(c^2 \nabla \times \vec{B}^{n+\frac{1}{2}} - \frac{1}{\epsilon_0}\vec{J}^{n+\frac{1}{2}}) \tag{3.10}$$

$$\vec{B}^{n+\frac{1}{2}} = \vec{B}^{n-\frac{1}{2}} - \Delta t(\nabla \times \vec{E}^{n}) \tag{3.11}$$

where $\vec{J}^{n+\frac{1}{2}} \equiv \frac{\sum_\alpha q_\alpha \vec{v}_\alpha^{n+\frac{1}{2}}}{\Delta x \Delta y}$ depends on the velocity. The updated velocity for each particle is calculated through the force from eq. (3.5).

$$\frac{v_\alpha^{n+\frac{1}{2}} - v_\alpha^{n-\frac{1}{2}}}{\Delta t} = \frac{q}{m}[E_\alpha^n + \frac{v_\alpha^{n+\frac{1}{2}} + v_\alpha^{n+\frac{1}{2}}}{2} \times B_\alpha^n] \tag{3.12}$$

The α subscript indicates the quantities are calculated for each particle; thus, the fields are smoothed out by the shape factor (e.g. $E_\alpha^n \equiv \int E^n S_3(x - x_\alpha, y - y_\alpha, z - z_\alpha) dx\, dy\, dz$). In practice, eqs. (3.10) and (3.11) are broken up into half-steps so that the electric and magnetic field are known for all half-steps. At first glance, eq. (3.12) does not appear to have an explicit solution for $v^{n+\frac{1}{2}}$. There are implicit methods that can solve this equation which are used in codes like Large Scale Plasma: An implicit particle-in-cell code (LSP) [74]. It turns out that there is an explicit solution given by the *Boris Rotation Algorithm*. If we define

$$v^{n+\frac{1}{2}} = v^+ + \frac{qE^n}{2m}\Delta t \tag{3.13}$$

$$v^{n-\frac{1}{2}} = v^- - \frac{qE^n}{2m}\Delta t \tag{3.14}$$

we can separate out the electric field dependence to get

$$\frac{v^+ - v^-}{\Delta t} = \frac{q}{m}[\frac{v^+ + v^-}{2} \times B] \tag{3.15}$$

which can conveniently be calculated through a rotation [72] through the following steps:

1. Compute v^- from eq. (3.14).
2. Compute $\vec{t} \equiv \frac{q\Delta t}{2m}\vec{B}^n$ (equivalent in magnitude to $\tan(\theta/2)$ where θ is the rotation angle)
3. Compute $\vec{s} = \frac{2\vec{t}}{1+t^2}$ (equivalent in magnitude to $\sin(\theta/2)$)
4. Compute $\vec{v}' = \vec{v}^- + \vec{v}^- \times \vec{t}$.
5. Compute $\vec{v}^{n+\frac{1}{2}}$ from eq. (3.13).

Now, the particles can be advanced or "pushed" from

$$x^{n+1} = x^n + v^{n+\frac{1}{2}}\Delta t \tag{3.16}$$

For completeness, the velocity initially needs to be pushed backwards from $v^0 \rightarrow v^{-\frac{1}{2}}$. This is not done in a time-centered way, but is only needed at the start of the simulation.

3.1.3 EPOCH Code

Clearly Top-hat shape functions should never be used for laser-solid simulations.

Background

Methods

Results

3.2 Machine Learning

3.2.1 Simple Models

Polynomial Regression

Support Vector Regression

3.2.2 Advanced Models

Gaussian Process

3.2.3 Neural Networks

Chapter 4

Particle-in-Cell Simulations of Enhanced Target Normal Sheath Acceleration

This chapter details the work I did in conducting PIC simulations to better understand the eTNSA mechanism that our group tried to demonstrate using LLNL's Titan Laser in March of 2024. As a result, I will mostly focus on the simulation aspect, but include some relevant comparisons to the experiment.

4.1 Theory

4.1.1 Spatially Aligned Pulses

As explained in section 2.2.1, there is generally an optimal level of pre-expansion of the target to maximize the TNSA proton energies [67, 75]. While this could be attributed to a low contrast pulse, this could also be an artificially injected pre-pulse whose intensity and temporal delay are tunable. Robinson et. al. [76] first addresses the idea of using multiple high intensity 40 fs laser pulses with the first being one-tenth to one-quarter of the intensity of the second. They termed this novel two-stage process "multiple pulse sheath acceleration". This study actually found a reduction in peak proton energy through numerical simulations, but did find the existence of "spectral peaks" – spikes in the energy spectrum as specific energies. A few years later, Markey et. al. [12] examined a similar setup experimentally, varying the temporal separation by 0.75-2.5 ps. Interestingly, they found an enhancement in the peak proton energy with a 0.75 ps separation and pulse energy ratio of 0.4:1. They conducted 1D PIC simulations shown in fig. 4.1 that verify this as well.

In 2018, Ferri et. al. [68] re-examines the same question, but uses the same intensity for both pulses. He finds that ultimately, little to no delay is optimal and as the delay gets larger, the enhancement reduces to the single pulse result. He finds the acceleration process can be affected by the second pulse for time delays as long as 0.6 ps for 3 μm targets and

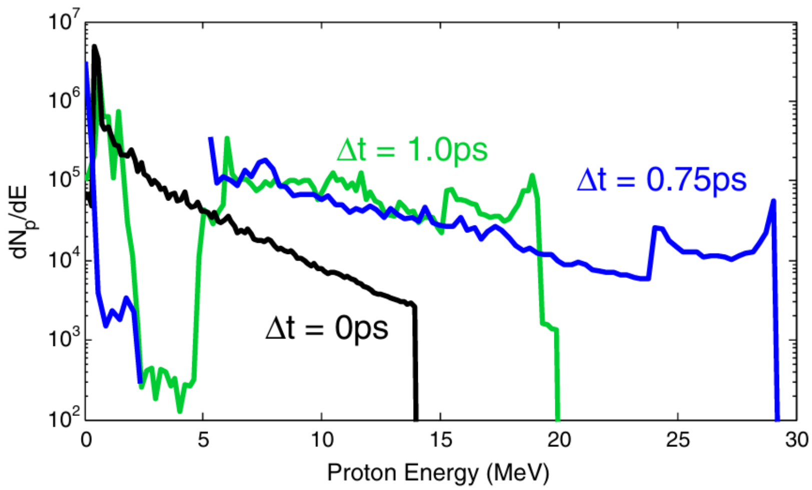

Figure 4.1: Proton energy spectrum from 1D PIC simulations depicted for three different temporal delays (including $\Delta t = 0$) from FIG. 3 in Markey et. al. [12].

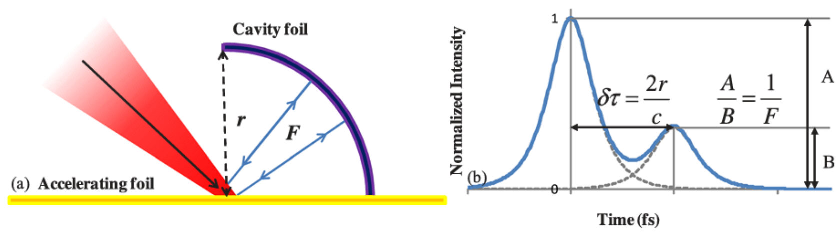

Figure 4.2: Schematic of the incident laser on the half-cavity target (left) in Scott et. al. [13]. The radius of the cavity foil determines the delay ($\tau = 2r/c$) between the main pulse and the post-pulse (reflected laser light of $\sim 40\%$) energy of the main pulse).

1 ps for 6 µm targets.

In a different approach Scott et. al. [13] realized that much of the laser light that is reflected is wasted, so a mechanism to re-direct this light back into the target would be desired. They designed a target with a half-cavity foil as seen in fig. 4.2 that will take light reflected off the accelerating foil and re-reflect it back towards the accelerating foil. They find that this can increase the laser to proton energy efficiency by up to $\sim 55\%$.

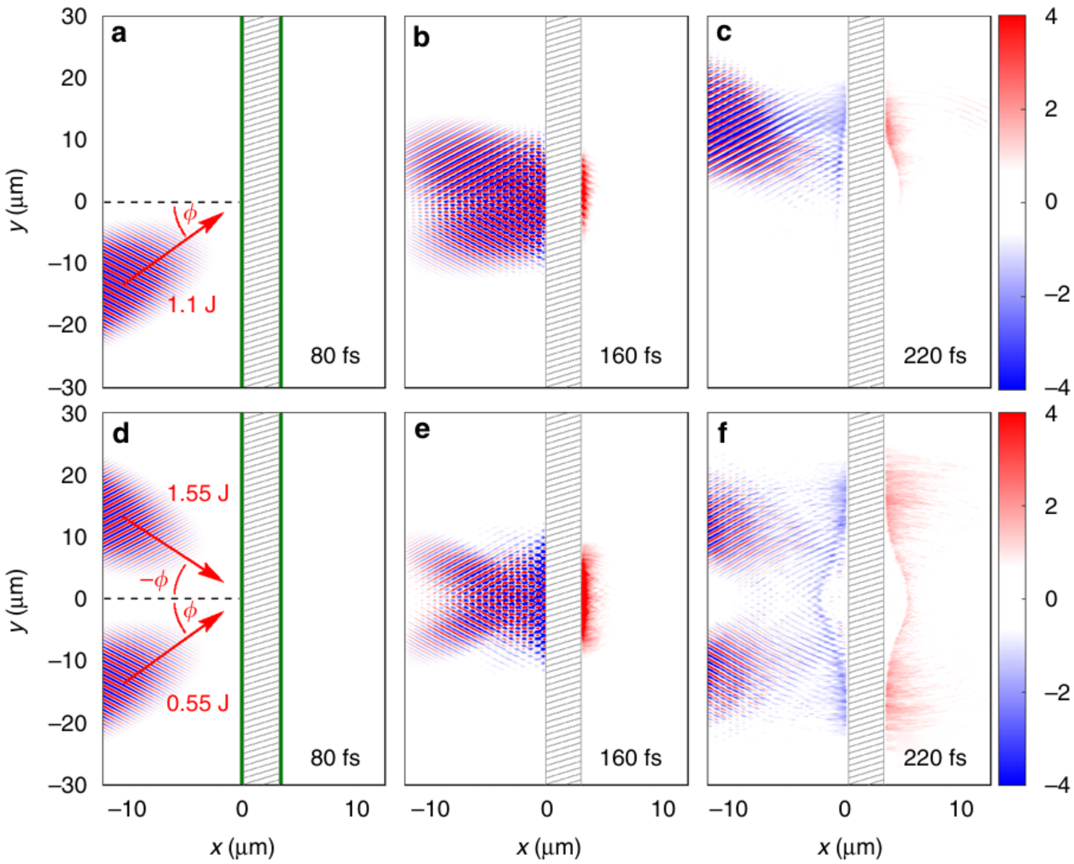

Figure 4.3: Geometry of the two pulse scheme as shown in FIG. 1 of Ferri et. al. (2019) [14]. The single pulse has a total energy of 1.1J at an incidence angle of $\phi = 45°$ and is shown through several time snapshots (a-c). In (d-f), the double pulse is shown through those same time snapshots with energies of 0.55 J in each pulse (the 1.55 J is a typo from the original figure). Other parameters includde $\tau_{\mathrm{fwhm}} = 38\,\mathrm{fs}$, thickness $= 3\,\mu\mathrm{m}$, material $=$ aluminum, $w_{0,\mathrm{fwhm}} = 5\,\mu\mathrm{m}$, $I_0 = 7 \times 10^{19}\,\mathrm{W\,cm^{-2}}$.

4.1.2 Spatially and Temporally Aligned Pulses

Ferri

Given the results of the previous section [12, 13, 68] that use short-delay pre or post pulses, Ferri decided to study how a spatially *and* temporally aligned pulse can enhance proton acceleration. Ferri, Siminos, and Fulop showed that the double pulse setup can result in an almost doubling of the proton energy and five-fold enhancement in the number of protons [14] through PIC simulations. This phenomena, referred to as eTNSA, is depicted in fig. 4.3 which shows the constructive interference of the fields at the front of the target in the center panel (e) and enhanced TNSA fields at the target rear (f).

The constructive interference of the electric fields can be understood by considering the electric field of two p-polarized pulses coming in at angles of incidence ϕ and $-\phi$

$$E_{x,1} = -E_0 \sin(\phi) \sin(ky \sin(\phi) - \omega t + kx \cos(\phi)) \tag{4.1}$$

$$E_{x,2} = -E_0 \sin(\phi) \sin(ky \sin(\phi) - \omega t - kx \cos(\phi)) \tag{4.2}$$

Adding these two fields together results in

$$E_{\text{double}} = -2E_0 \sin(\phi) \sin(ky \sin(\phi) - \omega t) \cos(kx \cos(\phi)) \tag{4.3}$$

which has an amplitude of $|E_{\text{double}}| = 2E_0 \sin(\phi)$. In contrast, a single pulse with twice the energy (intensity) would only have a $\sqrt{2}$ larger electric field ($|E_{\text{single}}| = \sqrt{2}E_0 \sin(\phi)$) which explains the enhanced electric fields seen in the bottom row of fig. 4.3. In an ideal situation where 100 % of the laser pulse is reflected, the angles of the two pulses do not need to be equal and opposite – we will get a standing wave pattern from the constructive interference of the incident wave with its reflection and the same $\sqrt{2}$ field enhancement.

Unlike the methods described in section 4.1.1 (which see enhanced proton acceleration from a pre-expanded target), eTNSA relies on the presence of an undisturbed target from the vacuum heating mechanism [8] explained in section 2.1.4. Vacuum heating relies on the dominance of the electron's quiver motion in the oscillatory electric field in the x-direction, but the magnetic field (which is relevant when $a_0 \gtrsim 1$) may impart a $\vec{v} \times \vec{B}$ Lorentz force (eq. (2.5)) that negatively affects the electron acceleration in the x-direction. Brunel even assumes in his original 1987 paper [8] that we can ignore $\vec{v} \times \vec{B}$ interactions if the laser is split into two equal and opposite angle pulses. Ferri confirms [14], through simulations, that the magnetic field is indeed suppressed in the double pulse case which results in hot electrons accelerated to higher energies.

Furthermore, Ferri performed some simulations that explored the effect of changing the preplasma scale length L at a fixed energy, and changing the total laser energy for the flat target [14] which can be seen in fig. 4.4. He finds that a higher preplasma scale length generally increases the max proton energy up to a certain scale length of around $L = 0.6\,\mu\text{m}$. The enhancement is seen for all scale lengths, but the gap between single and double pulse diminishes for larger scale lengths. In the double pulse case, a more favorable scaling with laser energy is seen for both the hot electron temperature and maximum proton energy ($E_{0,\text{tot}}$ as opposed to $\sqrt{E_{0,\text{tot}}}$) when comparing double pulse against single. In addition, Ferri comments that, for pulses with total energy greater than 10 J, the proton layer on the rear side starts to entirely disconnect from the bulk of the target during the acceleration, causing proton energies to saturate and become lower than the expected linear scaling.

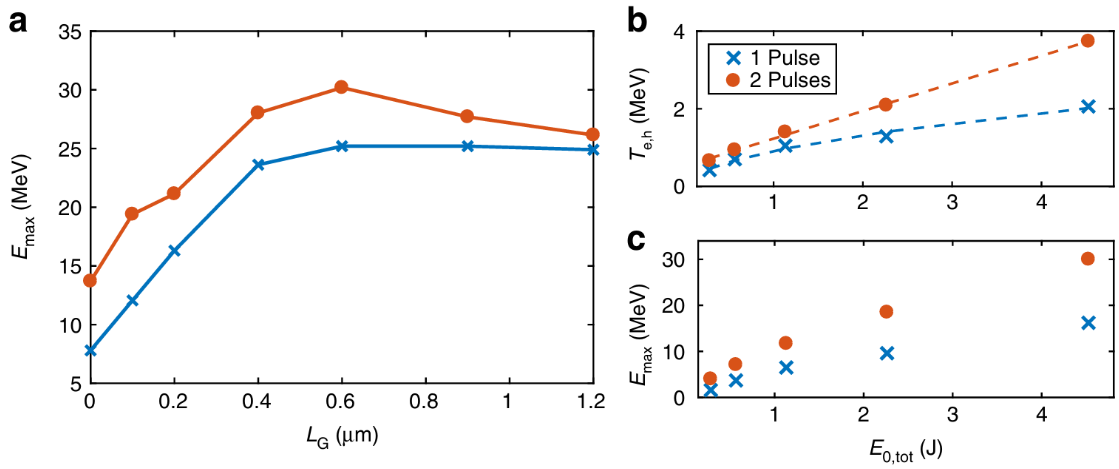

Figure 4.4: Double pulse effectiveness in terms of changing preplasma scale length (a) and total laser energy (b,c) from Ferri et. al. (2019) [14].

Other Simulations

In 2021, eTNSA was again demonstrated through simulations in Rahman et. al. [77] for a mJ class laser, around 2 orders of magnitude lower energy than the setup in Ferri's work. This mJ class laser is based on the experimental facility at the Wright Patterson Air Force Base (see chapter 6 for more details) which utilizes a thinner target of $\sim 460\,\mathrm{nm}$. Despite the major difference in laser and target parameters, the findings are similar – increased hot electron temperature and proton energies with double pulse compared to single pulse. However, Rahman finds that the presence of a preplasma actually *reduces* the maximum proton energy. But, like Ferri et. al., the gap between single and double pulse becomes smaller in the presence of a preplasma.

In 2024, Khan and Saxena [78] revisit the double pulse scheme but with an applied longitudinal kilo-Tesla level magnetic field. The purpose of the magnetic field is to reduce the divergence of the hot electron beam. This guides the electrons and enhances the TNSA process to see a higher maximum cutoff energy in the proton spectrum [79]. In this study, the laser was based off of the experimental set-up at the Rutherford Appleton Lab with a peak intensity of $5.5 \times 10^{20}\,\mathrm{W\,cm^{-2}}$ incident on a $7\,\mu\mathrm{m}$ polyethelene target.

Experiments

Due to multiple studies demonstrating eTNSA [14, 77, 78], experiments are needed to validate the PIC simulations. Morace et al. [80] showed that splitting a 270 J beam ($2.5 \times 10^{18}\,\mathrm{W\,cm^{-2}}$ peak intensity) into multiple "beamlets" on Al foil targets enhances

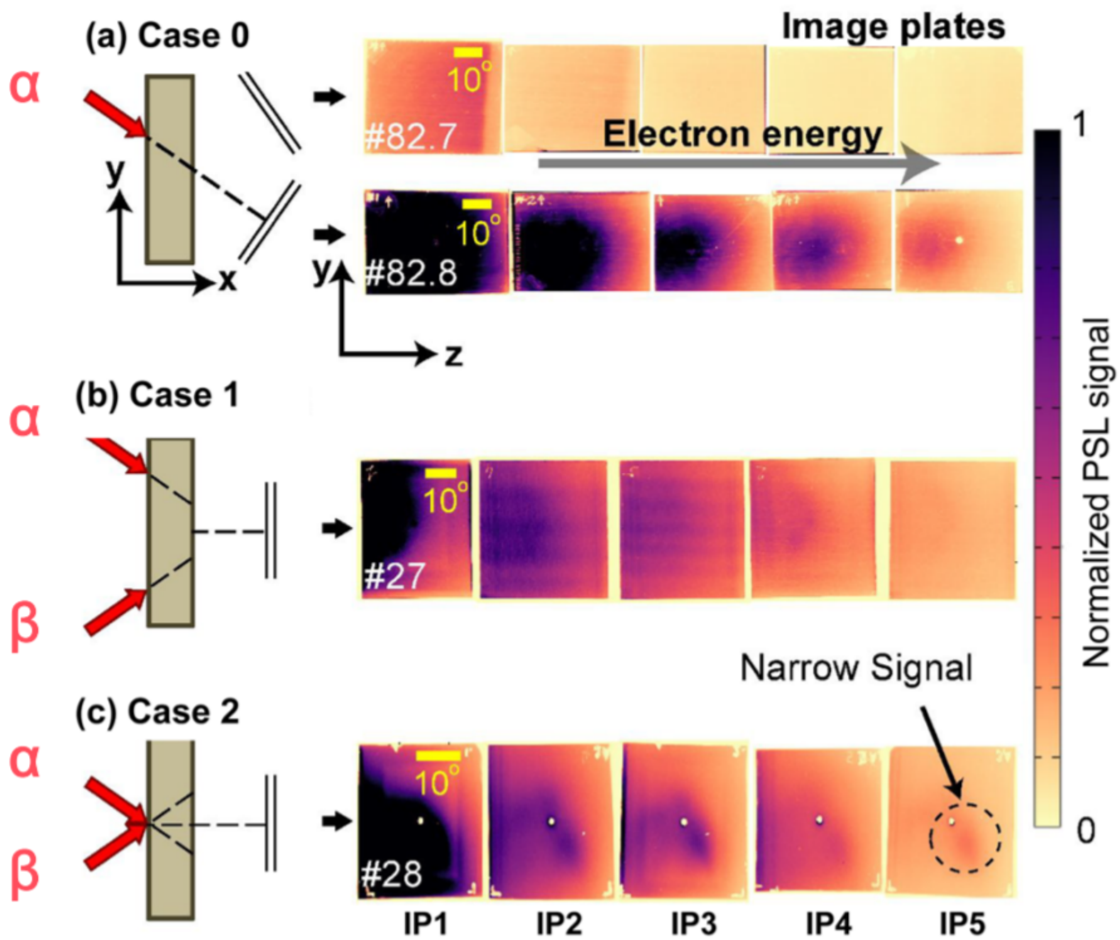

Figure 4.5: FIG. 2 from Yao et al. [15]. Case 0 shows electron signals from a single pulse. Case 1 shows electron signals from a double pulse with spatial separation 120 µm. Case 2 shows electron signals from a double pulse with no spatial separation.

the proton energy spectrum. These beamlets (dependent on the incidence angle) induced critical surface density modulations that strongly improved absorption into hot electrons.

Yao et al. [15] investigated the double pulse effect by changing the transverse spatial separation between two temporally aligned pulses as shown in fig. 4.5. This figure shows two possible beams α and β which come in at equal and opposite incidence angles with α angled in the $-y$ direction. Comparing (b) and (c) shows an enhancement of the double pulse electron energy when the pulses are spatially overlapped. In (a), the electron energy is recorded along the laser beam axis in contrast to (b) and (c) and this shows that most the electrons are getting accelerated along the laser beam axis. This suggests that the $\vec{J} \times \vec{B}$ mechanism is taking place (in contrast to vacuum heating or resonance absorption which drives electrons in the target normal direction). In terms of the protons, case 2 (spatially aligned double pulses) shows a more collimated central small beam which is absent in case 1 (spatially offset double pulses).

4.2 Results

Morace et. al. [80] was able to provide evidence ... Yao et. al. [15] was supported double pulse but didn't do a direct comparison with single pulse. Not enough experimental results out there, so we did an experiment ...

4.3 Discussion

Chapter 5
Machine Learning Methods Applied to Synthetic Ion Acceleration Data

In recent years, the application of ML methods to high energy density science (HEDS) has exploded due to two main reasons. First, ultra-intense laser systems are now capable of firing many shots per second and also collecting data at a similar rate. This allows scientists to collect a lot of data, which cannot reasonably be handled in real-time by a human. Second, machine learning frameworks like PyTorch [81] are easily accessible and powerful so that scientists who are not machine learning researchers are capable of using them.

One approach to applying machine learning with a limited amount of data is bayesian optimization (BO). BO, based on prior collected data points, attempts to find another suitable data point that is different than the prior data and expected to yield a more optimized output (according to some chosen criteria). Using BO, Jalas et al. [82] optimizes the quality of a laser-accelerated electron beam and Dolier et al. [83] optimizes the maximum proton energy using PIC simulations. Another notable effort is Loughran et al. [84] who used this approach to demonstrate higher maximum cutoff proton energies from an experiment using a 1 Hz laser. While this approach is commendable, it does not scale well to laser repetition rates of 100 or more Hz.

Quite a few works have explored using neural networks to analyze and extract information from large datasets generated from PIC simulations. Djordevic et al. [85] used these simulations to find an empirical estimate for the effective acceleration time by using a neural network model (NN) model (which informs our choice of 1.3 in Equation 5.20). Schmitz et al. [86] also trained NNs on PIC simulation data to better understand optimal laser and target parameter combinations for their system at TU Darmstadt. One thing these studies have in common is that they only use data from PIC simulations which don't necessarily reflect real experiments (especially so because they are 1D and 2D simulations with reduced dimensionality).

The Extreme Light Laboratory at the Wright-Patterson Air Force Base (WP-ELL) has a (1 kHz, $\tau_{\mathrm{FWHM}} = 40$ fs, $\lambda = 0.8\,\mu\mathrm{m}$, $w_0 = 1.5\,\mu\mathrm{m}$) mJ class laser that can currently collect ion spectrometer data at a maximum rate of 100 Hz [87]. Currently, the liquid target can be sustained for around 45 minutes before needing to be refilled which could theoretically result in 270,000 unique data points during one collection. Laser systems like this are still new and the stability of the liquid target often interferes with the goal of collecting quality data. As a result, we first focused our energy into doing a ML analysis on data produced from a well-known model by Fuchs [69] based on parameters at WP-ELL. The goal of this analysis is not to make recommendations as to what input parameters should be used in experiment, but to provide a general framework that can be extended to real data and also to help others incorporate ML in their work by sharing our code (see Zenodo [88, 89] for the python code and datasets). By providing these files we hope to encourage others to compare other ML models against our results as a benchmark. This chapter details the work I did developing this synthetic dataset, comparing different ML algorithms, and evaluating their potential effectiveness in a real experiment.

5.1 Modified Fuchs et. al. Model

In this section, I will describe the model from which we generated the synthetic datasets [17, 19]. First, the expansion of a plasma into a vacuum [16] is used to determine the maximum proton energy and the number of accelerated protons per unit energy $\frac{dN}{dE}$. Following Fuchs [69], we define the acceleration time in proportion to the pulse duration of the laser and adopt a scaling (e.g. eq. (2.33)) to relate hot electron temperature to the ponderomotive potential. This, in combination with other empirical estimates, allows calculating a proton energy spectrum from up to 7 parameters: main pulse intensity, contrast, wavelength, pulse duration, target thickness, target focal position, and laser spot size.

5.1.1 Plasma Expansion into a Vacuum

This model was developed by Mora [16] in 2003 who built off of earlier efforts [47, 48] in examining an isothermal expansion model. The model begins with the assumption that ions are contained in the semi-infinite interval $n_i = n_{i0}$ for $x < 0$ and no ions initially in the vacuum region for $x > 0$. The electrons are distributed according to the boltzmann relation given by eq. (2.20) where $n_{e0} = n_e(x = -\infty)$ is the electron density in the unperturbed plasma. Through this relation, $\phi(-\infty) = 0$. The initial electron density is related to the ion density $n_{e0} = Zn_{i0}$ where Z is the ion charge number for a fully ionized plasma. The potential also satisfies the Poisson equation eq. (2.4) where $\rho/m = -e(n_e - Zn_i)$ is the mass density of the electrons. The solution of eq. (2.4) at $t = 0$ is found by integration [47] (where $E \equiv -\frac{d\phi}{dx}$) as

$$\frac{1}{2}\epsilon_0 E^2 = n_{e0} k_B T_e \begin{cases} \exp(\frac{e\phi}{k_B T_e} - 1 - \frac{e\phi}{k_B T_e}) & \text{if x} < 0 \\ \exp(\frac{e\phi}{k_B T_e}) & \text{if x} > 0 \end{cases} \tag{5.1}$$

From enforcing continuity of eq. (5.1) at $x = 0$ (the location of the ion front initially) we determine $\phi = -k_B T_e/e$ to arrive at

$$E_{front,0} = \sqrt{\frac{2}{\exp(1)}} E_0 \tag{5.2}$$

where $E_0 \equiv \sqrt{n_{e0} k_B T_e/\epsilon_0}$. To get an estimate of the electric field at the ion front when $t > 0$ we need to consider what the characteristic time scale for ion motion is: the plasma ion frequency $\omega_{p,i}$

$$\omega_{p,i} \equiv \sqrt{\frac{Z n_{e0} e^2}{m_i \epsilon_0}} \tag{5.3}$$

which is analogous to eq. (2.15) So, in relation to the time-scale of plasma ion oscillations, a long time would refer to $\omega_{p,i} t \gg 1$. The ion fluid sound speed c_s is given by

$$c_s = \sqrt{\frac{Z k_B T_e}{m_i}} \tag{5.4}$$

and which is very similar to eq. (2.16) Using the definition of the debye length (eq. (2.17)) and sound speed c_s we can re-express eq. (5.3) as

$$\omega_{p,i} t = \sqrt{\frac{Z k_B T_e}{m_i}} \sqrt{\frac{n_{e0} e^2}{\epsilon_0 k_B T_e}} t = (c_s t)(\lambda_{D0}) \tag{5.5}$$

where λ_{D0} is the initial Debye length and c_s is the ion sound speed. As we know from chapter 2, when λ_D is smaller than the characteristic length scale of a system, the quasi-neutrality condition for a plasma is satisfied. In this case, the length scale would be $c_s t$ and we can show that asserting the condition $\omega_{p,i} t > 1$ is equivalent to $\lambda_D < c_s t$. We can continue by incorporating equations of continuity and the Lorentz force (eq. (2.5)) which can be expressed as

$$\frac{\partial n_i}{\partial t} + v_i \frac{\partial n_i}{\partial x} = -n_i \frac{\partial v_i}{\partial x} \tag{5.6a}$$

$$\frac{\partial v_i}{\partial t} + v_i \frac{\partial v_i}{\partial x} = -\frac{Ze}{m_i} \frac{\partial V}{\partial x} \tag{5.6b}$$

This set of fluid equations can be solved numerically with the initial conditions for n_i, E, and $v_i = 0$, but it is more instructive to consider a "self-similar solution" that describes the ions moving with speed

$$v_i = c_s + x/t \tag{5.7}$$

for $x + c_s t > 0$. It is self-similar in the sense that the specific length and time scales are not important, only their ratio x/t. In this self-similar region, quasi-neutrality is maintained and the expanding electron density can be expressed as

$$n_e = Zn_i = n_{e0}\exp(-\frac{x}{c_s t} - 1) \tag{5.8}$$

By combining eqs. (5.6a), (5.6b), (5.7) and (5.8), we can arrive at a solution for the self-similar electric field in this quasi-neutral region

$$E_{SS} = \frac{m_i c_s}{Zet} = \frac{k_B T_e}{ec_s t} = \frac{E_0}{\omega_{p,i} t} \tag{5.9}$$

Physically, we can interpret this as a sheet of positive charge $\sigma = \epsilon_0 E_{SS}$ at $x = -c_s t$ and a sheet of negative charge $-\sigma$ at the plasma edge. The location of this plasma edge (i.e. the location of the ion front) can be roughly obtained by equating the local Debye length $\lambda_D = \lambda_{D0}\sqrt{n_{e0}/n_e}$ to the scale length $c_s t$.

$$x_{i,front} = c_s t[2\ln(\omega_{p,i} t) - 1] \tag{5.10}$$

and the ion velocity at the front can also be obtained

$$v_{i,front} = 2c_s \ln(\omega_{p,i} t) \tag{5.11}$$

The ion velocity can plug back into eq. (5.6b) to find out that $E_{\text{front,SS}} = 2E_{SS}$. Mora found an approximate solution to E_{front} that matches $E_{\text{front},0}$ and $E_{\text{front,SS}}$ in their respective cases ($t = 0$ and $\omega_{p,i} t \gg 1$) as

$$E_{front} \simeq \frac{2E_0}{\sqrt{2\exp(1) + (\omega_{p,i} t)^2}} \tag{5.12}$$

This formula not only reaches the correct values in the limiting cases, but also effectively interpolates in the intermediary regions (i.e. $\omega_{p,i} t \sim 1$) when compared to a numerical code that solves eqs. (5.6a) and (5.6b) without assuming a self-similar solution. In fig. 5.1a, we see the net charge density at some time $\omega_{pi} t = 50$ after the start of a 1D plasma expansion simulation. We can identify the -2σ with the fastest expanding electrons and the $+\sigma$ region next to it as the positive ions getting pulled along. In fig. 5.1b, we can see the electric field between these two charged regions peaks $\simeq 2E_{ss}$. Then, using this formula with *eq.* (5.6b), we can determine the ion front velocity as

$$v_{i,front} = 2c_s \ln(\tau + \sqrt{\tau^2 + 1}) \tag{5.13}$$

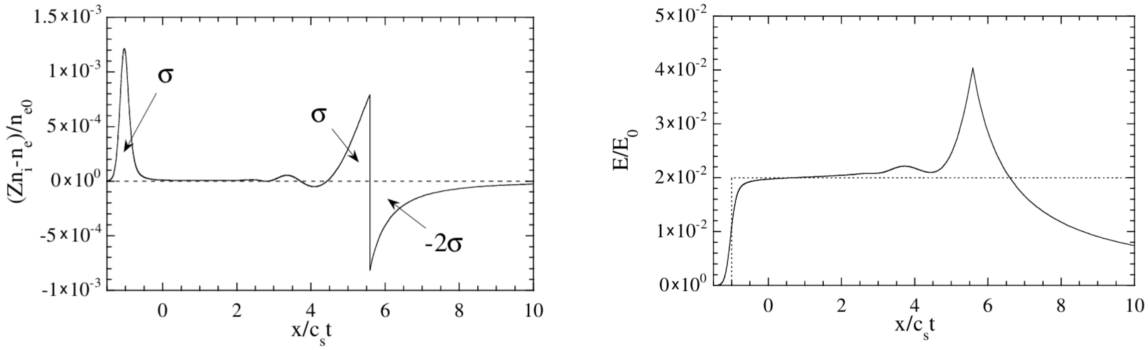

Figure 5.1: The net charge density (left) as a function of position x/c_st and normalized electric field E/E_0 (right) for $\omega_{pi}t = 50$ taken from Fig 1 and 2 in Mora's Paper [16]. On the right, the self-similar electric field from eq. (5.9) is plotted with a dashed line.

where we've defined a normalized acceleration time $\tau \equiv \omega_{p,i}t/\sqrt{2\exp(1)}$. Additionally, in the limit $\omega_{p,i}t \gg 1$, eq. (5.10) becomes

$$x_{i,front} \simeq c_st[2\ln(\omega_{p,i}t) + \ln(2) - 3] \tag{5.14}$$

The per-ion kinetic energy can now be calculated as

$$\begin{aligned}\mathcal{E} \equiv \frac{1}{2}m_iv_{i,front}^2 &= 2m_ic_s^2\ln(\tau + \sqrt{\tau^2+1})^2 \\ &= 2Zk_BT_e\ln(\tau + \sqrt{\tau^2+1})^2\end{aligned} \tag{5.15}$$

Using eq. (5.8), we can determine the number of accelerated ions between $x = -c_st$ and $x = x$ as

$$N_i \equiv \int_{-c_st}^{x} n_i(x')dx' = n_{i0}c_st[1 - \exp(-\frac{x}{c_st} - 1)] \tag{5.16}$$

and using eq. (5.7), we can show that this is equivalent to

$$N_i(x) = n_{i0}c_st[1 - \exp(-\sqrt{\frac{2\mathcal{E}}{\mathcal{E}_0}})] \tag{5.17}$$

where $\mathcal{E}_0 \equiv Zk_BT_e$. Now that the number of ions is expressed in terms of the energy $\mathcal{E}$, we can determine the number of accelerated ions per unit energy (per unit surface) as

$$\frac{dN}{d\mathcal{E}} = \frac{n_{i0}c_st}{\sqrt{2\mathcal{E}\mathcal{E}_0}}\exp(-\sqrt{\frac{2\mathcal{E}}{\mathcal{E}_0}}) \tag{5.18}$$

5.1.2 Modified Fuchs Model

When $\tau \to \infty$, eq. (5.15) diverges to ∞. This is an inherent limitation of the isothermal fluid model, and different models are able to avoid this issue [56, 90, 91]. However, a simple fix to this model involves assuming that this acceleration time is finite and proportional to the pulse duration. Physically, it makes sense that the protons are only getting accelerated on the timescale of laser-target interactions. This is the approach taken by Fuchs [69] and he expresses eq. (5.15) as

$$E_{\text{max}} = 2k_B T_h[\ln(t_p + \sqrt{t_p^2 + 1})]^2 \tag{5.19}$$

where $\tau \equiv \omega_{p,i} t_{\text{acc}} / \sqrt{2\exp(1)}$ just like the Mora model. We've also set $Z = 1$ to signify that we are looking for hydrogen ions (i.e. protons) The crucial difference is that we express the acceleration time as

$$t_{\text{acc}} \approx 1.3\tau_{\text{FWHM}} \tag{5.20}$$

One can assume that the absorption fraction of hot electrons η (with respect to the total laser energy E_L) is given by $\eta_e = 1.2 \times 10^{-15} I^{0.74}$ W cm^{-2} with a maximum of 0.5, determined from empirical scalings (e.g. see fig. 3 from Key [92]). Additionally, the average energy of the hot electrons is set by the Wilks scaling eq. (2.33). Putting this together,

$$N_e = \eta_e \frac{E_L}{T_h} \tag{5.21}$$

would be the total number of hot electrons accelerated into the target. These electrons spread out in a roughly cylindrical volume of area S_{sheath} and length $c\tau_t ext f whm$ where the circular sheath cross section can be estimated by $S_{\text{sheath}} = \pi(r_0 + d\tan(\theta))^2$. Here, $r_0 = w(x)\frac{\sqrt{2\ln(2)}}{2}$ is half of the (spatial) full width at half maximum of the intensity distribution at position x. The effective radius of the sheath has an additional factor of $d\tan(\theta)$ where d is the initial target thickness and θ is the half-angle divergence of the hot electrons within the target (taken as $\theta = 25°$). As a result, the hot electron number density can be expressed as

$$n_{e0} = \frac{N_e}{c\tau_{\text{fwhm}} S_{\text{sheath}}} \tag{5.22}$$

With an estimate of the hot electron density, the proton spectrum can now be computed from eq. (5.18) as

$$\frac{dN}{dE} = N_0 \frac{\exp(-\sqrt{2E/k_B T_h})}{\sqrt{2E k_B T_h}} \tag{5.23}$$

where $N_0 \equiv n_{e0} c_s t_{\text{acc}} S_{\text{sheath}}$ is defined for convenience. Using a dimensionless scale for energy $\varepsilon \equiv \sqrt{2E/k_B T_h}$, we can calculate the number of protons and total energy in protons through integrating eq. (5.23)

$$N = N_0(\exp(-\varepsilon_{\text{min}}) - \exp(-\varepsilon_{\text{max}})) \tag{5.24}$$

$$E_{\text{tot}} = N_0 \frac{k_B T_h}{2}[\exp(-\varepsilon_{\text{min}})(2 + \varepsilon_{\text{min}}(2 + \varepsilon_{\text{min}})) - \exp(-\varepsilon_{\text{max}})(2 + \varepsilon_{\text{max}}(2 + \varepsilon_{\text{max}}))] \tag{5.25}$$

where $\varepsilon_{\text{min}} = \sqrt{2E_{\text{min}}/k_B T_h}$ defines a minimum energy cutoff (ε_{max} is analogous and chosen by eq. (5.19)). Furthermore, we can calculate the average proton energy by dividing eq. (5.24) from eq. (5.25)

$$E_{\text{avg}} \equiv \frac{E_{\text{tot}}}{N} \tag{5.26}$$

The combination of eqs. (5.19) and (5.23) have been tested across many of the early TNSA experiments of the early 2000s for a wide range of laser intensities and pulse durations with good accuracy (see fig. 4 from Fuchs [69]).

5.1.3 Further Model Modifications

When restricted to a particular laser system, the wavelength, pulse duration, and spot size are fixed. Considering the model in section 5.1.2, only three adjustable parameters would be of interest – target thickness d, peak intensity I_0 and target focal position x. To introduce complexity into our model, we wanted to consider the effect that a pre-expanded target would have on the proton acceleration. The pre-expansion may enhance the hot electron generation, but expansion on the rear side of the target would reduce the effectiveness of the TNSA process. We incorporate this effect by allowing the laser to have a finite contrast κ which relates the intensity of the main laser pulse I_0 to the intensity of a secondary laser pre pulse as $I_{\text{pre}} = \kappa I_0$. This pre-pulse is treated as a spike in intensity that occurs t_0 before the arrival of the main pulse. The pre-expanded target would have a new effective thickness given by

$$d_{\text{eff}} = d + 2c_s t_0 \tag{5.27}$$

where c_s is the ion sound speed from eq. (5.4) in which the target is expanding outwards from both sides. Here T_e is the temperature due to the pre-pulse and can be calculated by assuming that $T_e \propto I$ and that an intensity of 10^{12} W cm^{-2} produces electron temperatures of $T_{\text{pre},0} = 50$ eV. Since n_e decreases as d gets larger and $\omega_{p,i} \propto \sqrt{n_e}$, eq. (5.19) is inversely proportional to the target thickness. So, a larger prepulse with a longer time to expand t_0

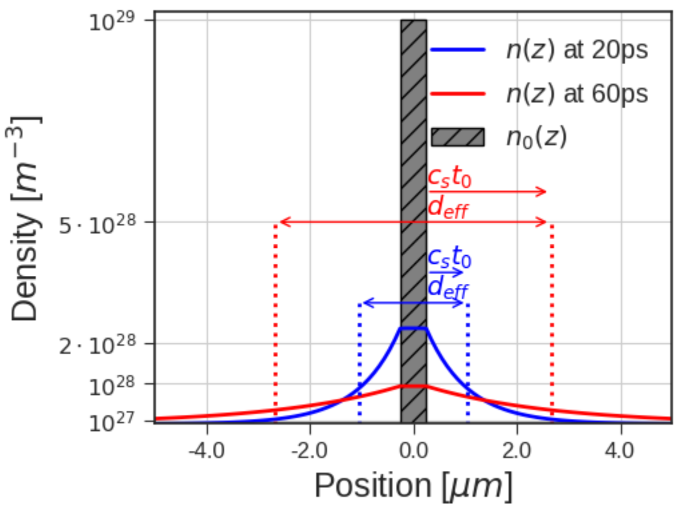

Figure 5.2: The electron density profile of the pre-expanded target is depicted for various times t_0. In this figure, $n(0) \equiv n_{\text{max}}$. Taken from Desai et al. [17] where z was used as the distance along the laser axis instead of x as done in this work.

will see a higher effective target thickness. Furthermore, when the target is off focus, the effective pre-pulse intensity on target is less which results in less expansion.

In addition, some of the main pulse energy can be depleted by traveling through the underdense region of this new pre-expanded target. These effects will be referred to as *pump depletion* and are inspired by arguments from Decker [93]. Decker describes pump depletion as an "etching" process where traveling through the plasma causes wavefront edge to recede at a speed given by the "etching velocity"

$$v_{\text{etch}} = (\omega_{p,e}/\omega)^2 c \tag{5.28}$$

Note that this speed continuously changes throughout the exponential-scale electron density which falls off like $n \sim \exp(-x/c_s t_0)$ on both sides of the target (see fig. 5.2 for a visual). Due to conservation of particle number, if the target expands, the maximum density $n$max will also lower and is given by $n_{\text{max}} = \frac{n_{e0} d}{d_{\text{eff}}}$. We can integrate v_{etch} with respect to time, but it is more convenient in terms of the position since we know the range over which the under-dense plasma exists. The plasma edge x_f is given by eq. (5.14) and we will integrate up to the location of the critical density $x_0 = c_s t_0(\ln(n_{\text{max}}) - \ln(n_c))$. Utilizing the change of variables $dx = cdt$ (due to the pulse traveling at the speed of light c), the "etching distance" can be calculated as [17]

$$L_{\text{etch}} \equiv \int_{x_0}^{x_f} v_{\text{etch}} \frac{1}{c} dx = \frac{e^2 n_{\text{max}} c_s t_0}{\epsilon_0 m_e \omega^2} \left(\exp\left(-\frac{x_0}{c_s t_0}\right) - \exp\left(-\frac{x_f}{c_s t_0}\right)\right) \tag{5.29}$$

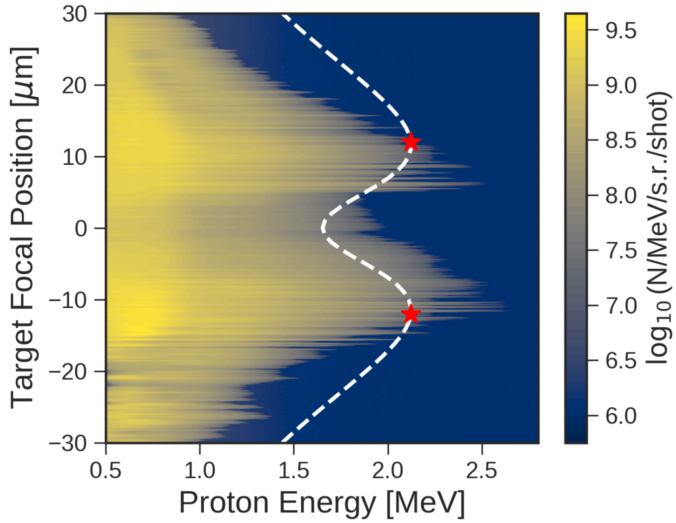

Figure 5.3: The dotted black line shows the maximum proton energy predicted by eq. (5.19) with the pump depletion considerations in section 5.1.3 assuming $t_0 = 60\,\text{ps}$, $I_0 = 10^{19}\text{W cm}^{-2}$, $\kappa = 10^{-7}$, $d = 0.5\,\mu\text{m}$. The red stars indicate the predicted positions of maximum proton energy $\sim 12\,\mu\text{m}$. This plot is overlayed on top of an experimental maximum proton energy distribution from Morrison et. al. [18]. This figure is taken from Desai et. al. [17].

Finally, this etching reduces the effective pulse duration by

$$\tau_{\text{fwhm,eff}} = \tau_{\text{fwhm}}(1 - \frac{L_{\text{etch}}}{c\tau_{\text{fwhm}}}) \tag{5.30}$$

This model, however, is not without its flaws. First, our calculations assume a critical density of a tenth of the amount of the actual critical density. Second, instead of defining $d_{\text{eff}} = d_0 + 2x_0$ (which would be the true effective density that remains above critical density), we substitute it with eq. (5.27). Third, we modify the multiplier seen in eq. (5.20) from 1.3 to 25 which is a significant departure. Finally, the proportionality $T_e \propto I$ with $T_{\text{pre},0} = 50$ eV is chosen arbitrarily. Despite these drawbacks, we obtain model predictions similar to what is seen in fig. 5.3 to account for the maximum proton energy dip at peak focus. The goal of creating this model modification is to add complexity to the underlying physics for the purposes of evaluating the effectiveness of machine learning models, not to invent new physics.

5.2 First Analysis

In this section, the results from my publication in *Contributions to Plasma Physics* [19] in November of 2024 will be discussed. This work started with the work of Joe Smith and Ricky Oropeza who first coded up the modified Fuchs et al. model in Python. Then, undergraduate student Tom Zhang did some preliminary work in exploring different ML frameworks to see what models could fit the data the best. I initially worked in a complementary fashion to Tom, but finished up the project after Tom graduated from OSU with some help from undergraduate student Jack Felice. Along the way we were supported by coauthors Alona Kryshchenko from California State University - Channel Islands (CSUCI) in addition to Anil Patnaik and Michael Dexter from Air Force Institute of Technology (AFIT). This work was modelled on the WP-ELL laser system described in et al. [87] with laser parameters mentioned in the beginning of chapter 5.

5.2.1 Methods

In this work, we explored a 25,000 point dataset based on the model described in subsection 5.1.2 which had three output quantities: $E_{\text{max}}, E_{\text{tot}}, E_{\text{avg}}$ **??**. We modified the acceleration time (in Equation 5.20) from 1.3 to 4 to better match the points in our dataset which is still within the range that Djordevic et al. [85] recommended. Three input quantities were varied: peak laser intensity I_0 (from 10^{18}W cm^{-2} to 10^{19}W cm^{-2}), target thickness d (from 0.5 µm to 5 µm), and distance from peak focus to the target x (from -30 µm to 30 µm). The input quantities were randomly chosen (uniformly within their intervals) with the Fuchs et al. model evaluations yielding the three outputs. To make the problem non-trivial, noise was added to the outputs sampled from a log-normal distribution with a mean of the output value and standard deviation between 0 and 30 % of the output value. Varying the noise, which would be present in an experimental dataset, will show how well a model can handle noise. Since we define the standard deviation as proportional to the mean (rather than some constant), the raw amount of noise becomes larger as the predictions get larger.

As a pre-processing step, we first applied a logarithm to both the intensity and three outputs of the model. This was necessary due to our choice of sampling the intensity uniformly with respect to the exponent (i.e. 18-19) and the output energies are directly proportional to the intensity. Additionally, we applied z-score normalization to both the inputs and outputs which is standard in machine learning algorithms to keep all data points on the same order of magnitude. From the 25,000 total points, we used 20,000 for training and reserved a hold-out set of 5,000 for testing. We determined the scalings from the training set only to ensure there is no leakage of information into the testing set. Furthermore, we multiplied the unscaled outputs by a correction factor equal to the mean of the training outputs divided by the unscaled outputs to reduce and under-predicting bias introduced by the log-scaling of the outputs [94].

We used three different ML models in our study: Support Vector Regression (SVR), gaussian process regression (GPR), NN that were programmed using RAPIDS [95], GPyTorch [96], and Skorch [97] respectively in Python. These packages all contain functions to

NN	BS = 256, leaky ReLU, $N_h = 3$, $N_l = 64$, Adam, LR = 0.001
SVR	$\epsilon = 0.01$, $C = 2.5$, tolerance = 0.001
GPR	Iterations = 30, LR = 0.001

Table 5.1: Average GPU memory consumption results when training on data with 20000 points.

facilitate running Graphics Processing Unit (GPU) accelerated scripts and were ran using the Pitzer cluster on the Ohio Supercomputer Center (OSC). All three approaches benefitted from hyperparameter optimization through the `GridSearchCV` module of scikit-learn. These choices are summarized in Table 5.1. For both the GPR and SVR, a Radial Basis Function (RBF) kernel was used.

5.2.2 Results

Our first task was to evaluate how well the trained models can fit the underlying dataset as the number of data points is increased. We accomplished this by evaluating the models on a testing set which is which is proportional to the amount of training points in a 80-20 training-testing split. In Figure 5.4, the MAPE is evaluated between the model outputs and the testing data outputs to assess the accuracy of each method for three different noise levels – 0, 15, and 30 %. Since, in this figure, the testing data contains noise, it is impossible to achieve 0 % error. As a result, we've included a black line to show the error between the testing data and the theoretical value predicted by the Fuchs et al. model. We can clearly see that the all the ML models don't appear to get better when we increase the number of data points. Additionally, we can see that the NN model has the worst accuracy and and more variability.

Then, we kept the number of data points fixed at 2000 and varied the noise level from 0 to 30 % and made a similar analysis in Figure 5.5. These plots show how the NN model doesn't do well without any noise. In addition to the noisy test data (solid line), the error with the same data without noise was also plotted as a dashed line. One interesting feature about this plot is that the NN model seems more resilient to noise in the sense that it does not increase very much as the noise level increases.

Next, we compared the execution time of the different ML models and found that the SVR runs the fastest, the GPR runs the slowest, and the NN runs at a speed somewhere in between. The GPR scales roughly as $\mathcal{O}(N^3)$ [98] which can be contrasted with the NNs $\mathcal{O}(N)$. In terms of GPU memory utilized, the GPR used the most at around 14 GB scaling [98], whereas the SVR and NN used between 1 and 2 GB. Due to the unfavorable $\mathcal{O}(N^2)$ memory scaling of the GPR [98], larger datasets than 40,000 points were practically infeasible with our implementation.

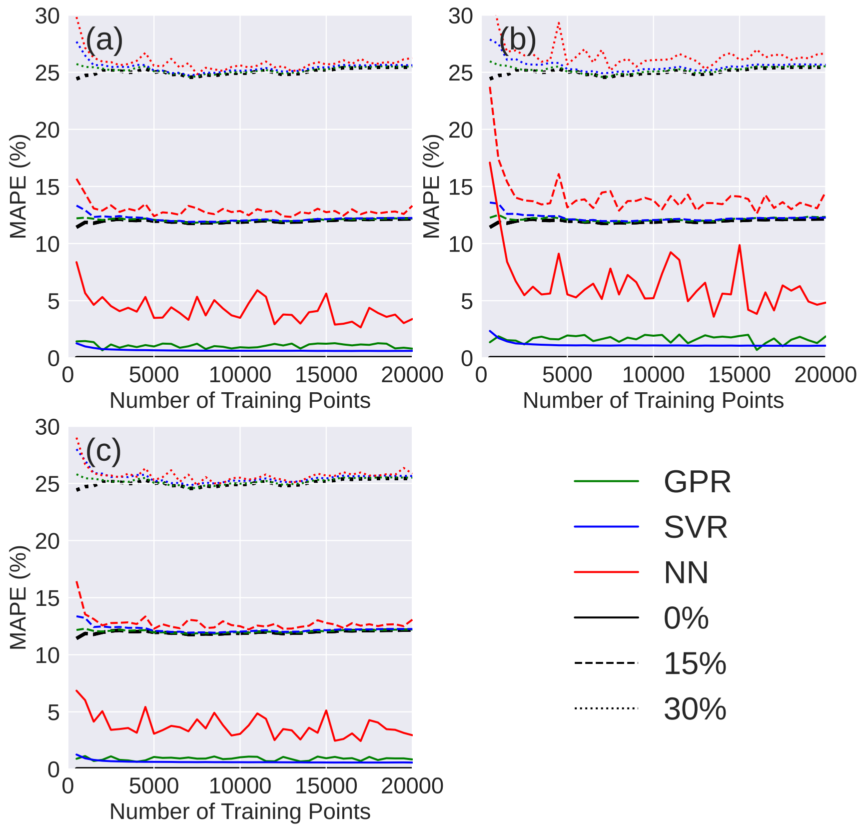

Figure 5.4: MAPE versus number of training points from ML model predictions for (a) max proton energy, (b) total proton energy, (c) average proton energy and noisy testing data. Each panel shows results from (solid) 0%, (dashed) 15% and (dotted) 30% added noise in the data. Black lines with different line types indicate the MAPE between the noisy and noiseless data. Because we only compare ML models to noisy data in this figure, these black lines indicate the best that any ML model could conceivably do. Figure and caption taken from Figure 3 of Desai et al. [19].

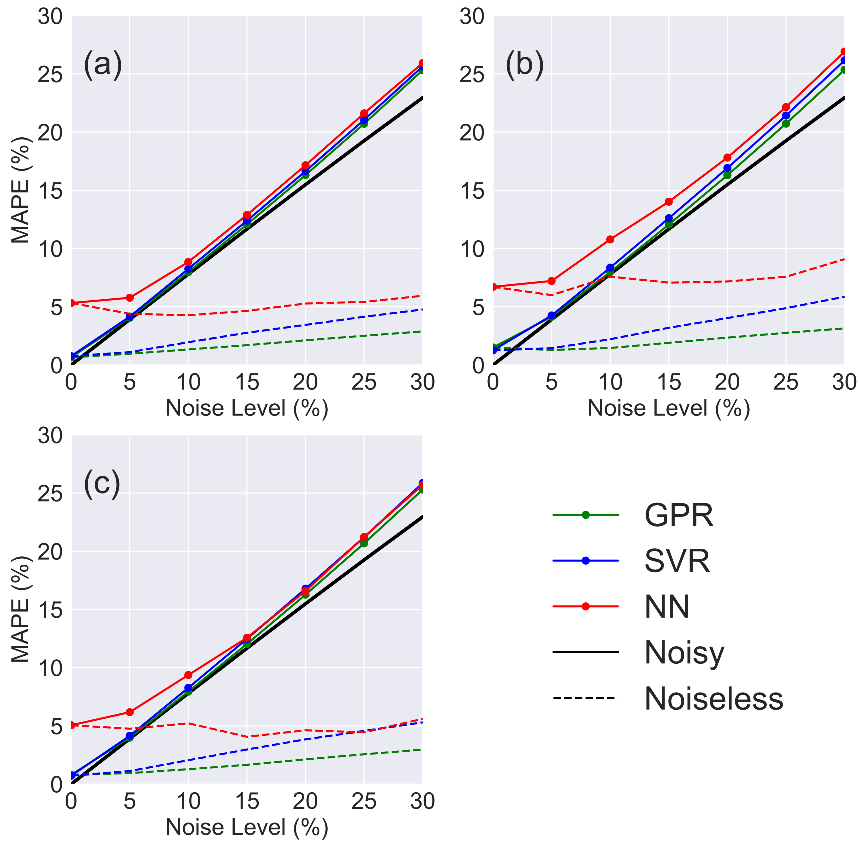

Figure 5.5: Solid lines show the typical MAPE in (a) maximum proton energy, (b) total proton energy, and (c) average proton energy when the ML models (which were trained on 2000 synthetic data points with noise) are evaluated on data with different levels of noise. Dashed lines show the typical error when those same ML models are evaluated on noiseless test data. Black solid lines indicate the MAPE between the noisy and noiseless data. Figure and caption taken from Figure 4 of Desai et al. [19].

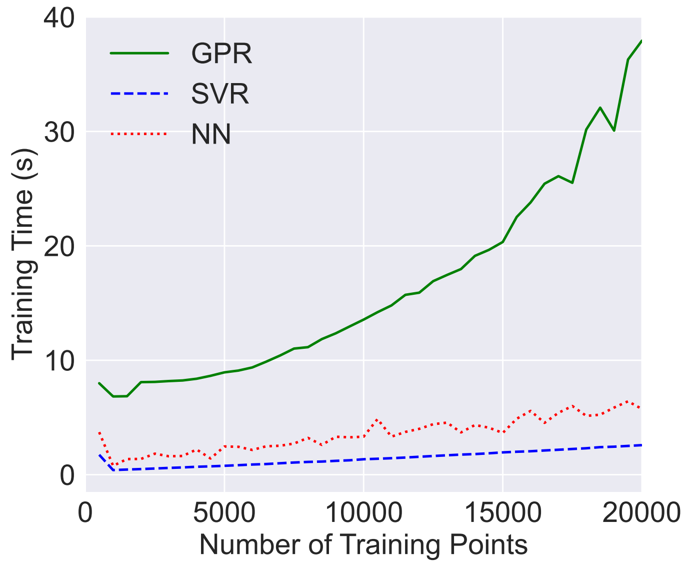

Figure 5.6: Comparing the execution time of the different ML models averaged across noise levels in computing the maximum, total, and average proton energies. Figure and caption taken from Figure 5 of Desai et al. [19].

5.2.3 Optimization Task

We highlighted a useful application of these models by designing an optimization task – to determine a set of inputs that would produce a proton energy spectrum up to a specified maximum energy. Additionally, these inputs would correspond to a high number of proton in that energy range as well. We characterize the balance of these two quantities – the maximum cutoff energy KE_c (E_max) and the laser to proton conversion efficiency η_p ($E_\mathrm{tot}/E_\mathrm{laser}$) – as

$$f(KE_\mathrm{c}, \eta_p) = \frac{|KE_\mathrm{c} - KE_\mathrm{c,goal}|}{KE_\mathrm{c,goal}} + \frac{C}{\eta_p} + g(KE_\mathrm{c}, KE_\mathrm{c,goal}) \tag{5.31}$$

where C is a parameter that can influence the relative strength of η_p in comparison to KE_c. These features can seen in Figure 5.7 where three different energy cutoffs were chosen to optimize towards: 1, 0.5, and 0.25 MeV. The green region focuses on regions of the parameter space that closely match the given cutoff, while the blue region additionally factors in η_p. For practical reasons, we impose a penalty term $g(KE_\mathrm{c}, KE_\mathrm{c,\ goal})$ that prevents choosing points that have KE_c more than 15 % away from the specified cutoff. These plots are generated from the Fuchs et al. model with 0 added noise, so they should be regarded as the ideal results that can be compared with the ML models.

We generated the same plots as Figure 5.7 with trained ML models on 2000 training data points with 30 % added noise which can be seen in Figure 5.8. These results show

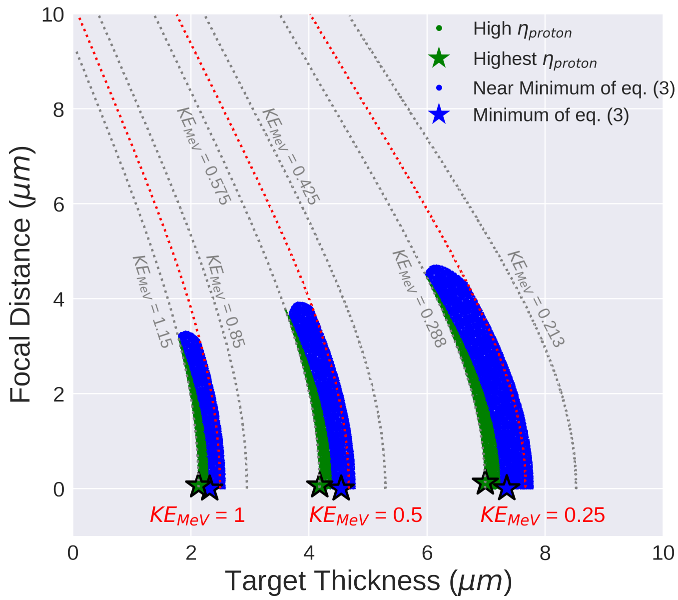

Figure 5.7: Parameters that produce maximum proton energy cutoffs in three different desired ranges: 1.0 MeV, 0.5 MeV and 0.25 MeV. Combinations of thickness and focal distance that produce these energy cutoffs (irrespective of the laser to proton conversion efficiency) are shown with dotted red lines. With each red line we also show with dotted gray lines the thicknesses and focal distances that produce proton energy cutoffs that are +15% or -15% of the cutoff goal. Green shaded areas show regions where the laser to proton conversion efficiency is high (i.e. within 5% of the optimal value). A green star shows the ideal conditions for maximizing the proton conversion efficiency. The blue region corresponds to using all the terms in Equation 5.31 and the blue star indicates the ideal conditions according to that minimization scheme. Figure and caption taken from Figure 6 of Desai et al. [19].

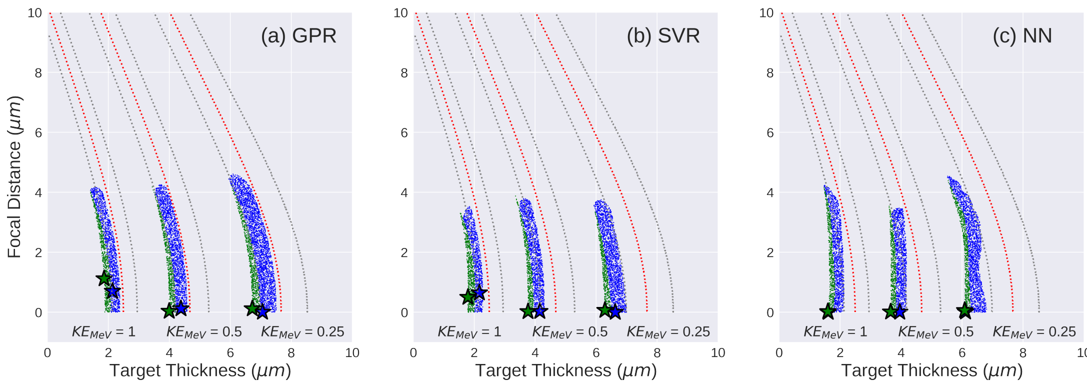

Figure 5.8: Parameters that produce maximum proton energy cutoffs according to three trained ML Models on 2000 data points with 30 % added noise: (a) GPR, (b) SVR, (c) NN compared against the red and gray lines plotted in Fig.5.7. The green and blue shaded regions are scatter plots of a subset of evaluated points that fall within 5 % of the model's predicted optimum according to the same criteria in Fig. 5.7. Figure and caption taken from Figure 7 of Desai et al. [19].

the GPR matching the closest to Figure 5.7 and the SVR performs almost as well. On the other hand, the NN clearly has more erratic shapes which is not surprising due to its lower accuracy from the preceding analysis in Figure 5.5.

5.3 Second Analysis

In this section, the work from section 5.2 was expanded upon and written into a manuscript that is currently under consideration at *APL Machine Learning*. This work was originally assigned to (then) undergraduate student Jack Felice as a similar, but complementary project to what I primarily worked on (described in section 5.2). Jack did the bulk of the work in this project and borrowed help from me as needed. When Jack left for graduate school at the University of Maryland, I spent a few months organizing his work, contributing to the text of the paper, and creating polished figures. The co-authors from this work are largely the same as the previous work, but additionally include fellow graduate student Nathaniel Tamminga for his discussion on the constrained data campaign. This work was also modeled on the WP-ELL laser system.

5.3.1 Methods

In section 5.2, we tried to address training a relatively small model on only 20,000 data points. Furthermore, this model was relatively simple – a regression algorithm could fit the model quite accurately with only a few thousand points. Also, we found that the NN model performed poorly due to lack of model complexity and too few data points. A real experimental dataset would be much more complex and thus require more data to understand its underlying trends. As a result, our second project added complexity in the form of pre-expansion of the target explained in subsection 5.1.3.

From this new modified model, we generated a training dataset of 1,525,000 points by sampling from a uniform grid of points in a 4D parameter space. The three inputs in section 5.2 are the same (except we reduced the maximum of the target thickness to 5 µm). This grid included thicknesses in steps of 0.5 µm, focal positions in steps of 1 µm and intensities in steps of 1.8×10^{17} W cm^{-2}. The relevant quantity to control the extent of the pre-plasma is the contrast κ which was varied in steps of 1.8×10^{-8}. In Figure 5.2, the effect of the prepulse can be seen modifying the density profile of the target ($t_0 = 60$ ps was used in this work). The 250,000 point testing dataset was generated from the same intervals as the training set, but without noise and on a grid of points (instead of random sampling throughout the interval).

We used the same outputs as before: E_{max}, E_{tot}, and E_{avg}. Since the new contrast parameter can make the proton energies get arbitrarily low, we set a floor to these outputs energies of 1 keV, 1 nJ, and 1 keV respectively. This was motivated by the finite energy resolution of ion energy detectors, but also by preventing the MAPE metric from getting a division by zero error. Additionally, the acceleration time multiplier (see Equation 5.20) was increased to 25 to balance out the lower predicted proton energies from the new physics model's larger effective thickness (Equation 5.27). The features of this new model can be seen in Figure 5.2 which highlight the characteristic "dip" in the proton energy at peak focus obtained from Morrison et al. [18].

Like the previous work in section 5.2, we used a NN model, but we modified the other two. Instead of the SVR, we used the more elementary polynomial regression (POLY) due to its simplicity which can be used as a baseline model without GPU accelerated computations. The data in section 5.2 could be fit accurately to a simple POLY model but, as we'll see later, does not work well with the added complexity in the new model. Then, we replaced the exact GPR with the stochastic variational gaussian process (SVGP) (see [99]) which assumes a variational distribution over some amount of inducing points, restricting the training data to a representative subset. This allows the SVGP to be trained on data sets of order one million points in mini-batches just like the NN. Like before, we summarize the hyperparameters in Table 5.2. Finally, we replaced the standard z-score normalization with min-max scaling – a linear scaling that scales the minimum value of a particular data column to be 0 and the maximum value to be 1. Min-max scaling was chosen to better represent the nature of parameter selection: uniform sampling between some minimum and maximum value.

NN	BS = 256, leaky ReLU, $N_h = 3$, $N_l = 64$, Adam, LR = 0.001
POLY	$\epsilon = 0.01$, $C = 2.5$, tolerance = 0.001
SVGP	Iterations = 30, LR = 0.001

Table 5.2: HPS TABLE

5.3.2 Results

In Figure 5.9a, the MAPE is calculated for each of the three ML models with a variable number of training data points from a dataset with 10 % added noise. The MAPE is evaluated on the fixed size testing dataset of 250,000 points. For the NN and SVGP models, 20 % of the training set was reserved as a validation set. Here, we can clearly see that the NN and SVGP have a significantly lower percentage error than the POLY. Additionally, Figure 5.9b shows that the SVGP takes significantly longer than the NN to train which takes significantly longer than the POLY (note the logarithmic scale).

Then, like in section 5.2, we analyzed the effect of changing the noise level in Figure 5.10. We can see that the POLY again has the worst accuracy which does not change with the noise level. While the SVGP and NN are more accurate, the SVGP seems to perform worse at a higher noise level.

5.3.3 Optimization Task

Similar to section 5.2, we came up with an optimization task to demonstrate the effectiveness of the models. This time, we used a slightly different objective function

$$f(KE_{\mathrm{c}}, \eta_p) = \frac{|KE_{\mathrm{c}} - KE_{\mathrm{c,goal}}|}{1\mathrm{MeV}}\beta - 100\eta_p(1-\beta) \tag{5.32}$$

which can be contrasted to Equation 5.31. One notable difference is the subtraction of the conversion efficiency η_{p} instead of adding $1/\eta_{\mathrm{p}}$. This allows us to control the relative strength of the two terms through a quantity β that varies from 0 to 1. Figure 5.11 shows the distribution of $\mathrm{KE_c}$ (i.e. E_{max}) and η_{p} (i.e. $E_{\mathrm{tot}}/E_{\mathrm{laser}}$) as a function of target thickness and focal position when fixing the intensity and contrast to the maximum and minimum within their respective ranges.

For our optimization task, we used the models trained on 30 % added noise to sample a set of points which fixes the laser energy at 14.14mJ (by assuming $I_0 = 10^{19}\mathrm{W\ cm^{-2}}$) and the contrast to $\kappa = 10^{-7}$, but varied the target thickness and focal distance. The thickness and focal distance were stepped in 0.1 µm increments to generate a 2D grid of 13,846 points to evaluate the trained models on. Notably, the step sizes are 5-10 times smaller than what was used in the dataset generation so that the models will be forced to interpolate between points not originally seen by the trained models.

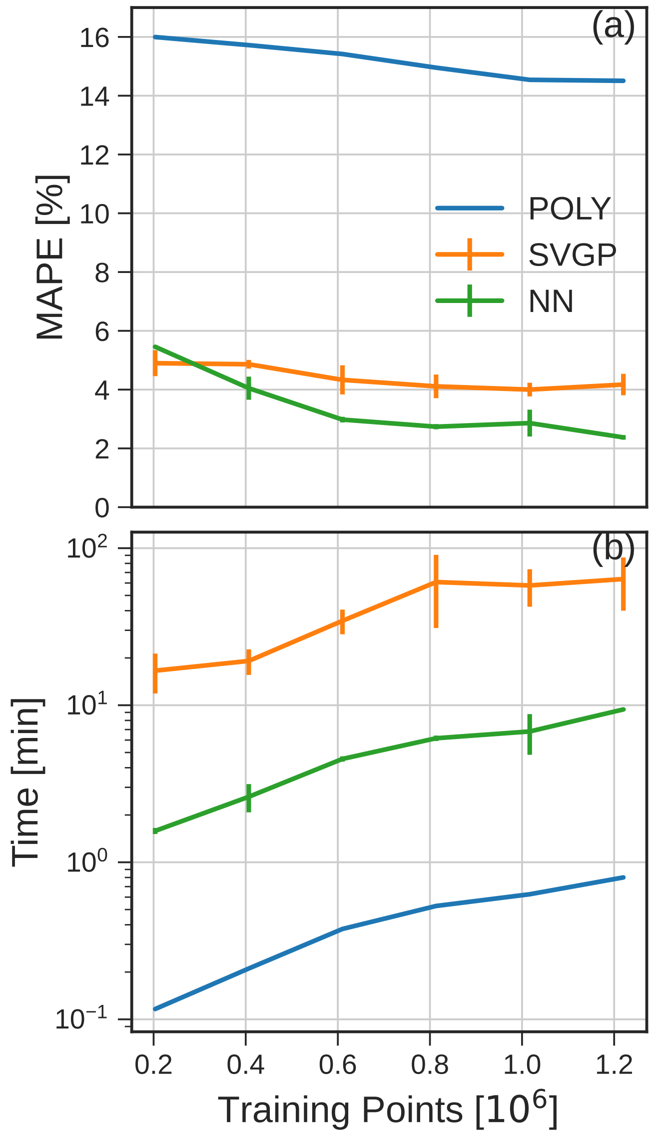

Figure 5.9: Model training results using data with 10 % added noise. Testing MAPE (a) is plotted for the three ML models against the number of training points and averaged between results for maximum, average, and total proton energy. The training time (b) of the ML models in minutes is plotted on a logarithmic scale. The vertical bars are standard deviations computed from running the training splits 3 times with different seeds to control the data splitting and random parameter initialization of the NN and SVGP models.

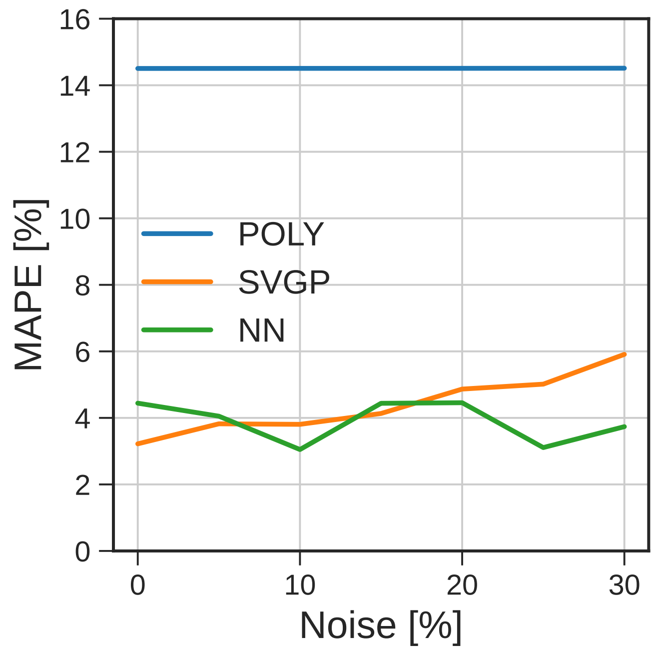

Figure 5.10: Testing MAPE is plotted against different levels of gaussian noise using the full training dataset for the three models with the three output energy results averaged.

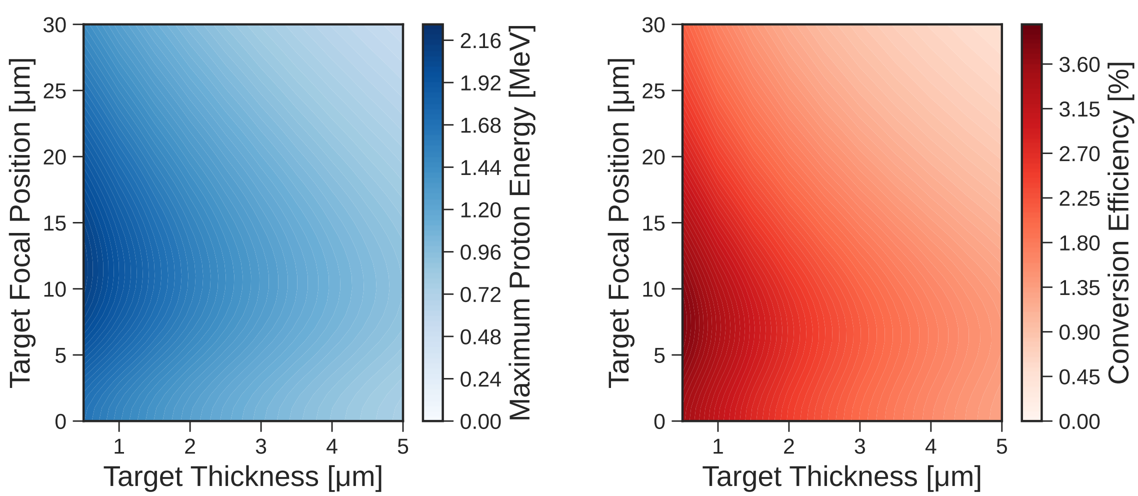

Figure 5.11: Colormaps in the 2D parameter space of target thickness and target focal position that display (left panel) the maximum proton energy (i.e. energy cutoff KE_c) and (right panel) laser to proton energy conversion efficiency η_p as calculated from the modified Fuchs et al model. These plots were generated assuming 14.14 mJ of laser energy and a pre-pulse contrast of 10^{-7}.

	β	0	0.25	0.5	0.75	1
RMSE	POLY	0.329	0.223	0.121	0.057	0.124
	SVGP	0.143	0.096	0.062	0.065	0.101
	NN	0.065	0.052	0.042	0.038	0.042
Δ_{opt} [μm]	POLY	4.5	5.5	7.5	9.489	2.121
	SVGP	3.5	4.5	5.601	4.148	4.144
	NN	0.4	1.2	3.1	0.825	4.717

Table 5.3: Comparison metrics evaluated from Figure 5.12. The RMSE row shows the root mean squared error between the colormap values of the ML models and the analytic model for each value of β. The Δ_{opt} row calculates the Euclidean distance between the predicted optimum and true optimum (i.e. distance in μm between the cyan and white stars in Figure 5.12).

The optimum conditions that minimize Equation 5.32 are indicated with a star in Figure 5.12 for a range of β values. In this analysis, the goal cutoff is fixed at $\text{KE}_{\text{c, goal}} = 1$ MeV, but this approach can easily be generalized to a different value. The upper panels of Figure 5.12 are the results from the analytic model (noiseless) and should be regarded as the true distribution of Equation 5.32. The optima of these panels are indicated with a white star. The other rows show the estimated distribution according to the three ML models and have an predicted optima shown with a cyan star. For comparison, the white star from the analytic model is overlayed on each panel.

In Figure 5.12, one can see that for $\beta = 0.25$, the best (i.e. globally minimum) region is at 0.5 μm thickness and 10 μm focal position, which correspond to regions with higher η_p. The POLY and SVGP models predict the optimal conditions to be at a focal position of ~ 15 μm, in contrast to the NN prediction of ~ 11 μm. In this case, the NN more closely matches the true optimum. For high values of β, the best region is a curve composed of points that closely match KE_{c} to $KE_{\text{c,goal}}$. Using the highest value of $\beta = 1$, we see that while the NN looks much less smooth, it fits the overall shape of the underlying Fuchs model better than the other two methods.

To quantify the features of Figure 5.12, we can look to Table 5.3. We can assess the accuracy in the optimal conditions by taking the Euclidean distance in the focal position - target thickness space between the true optimum conditions and the ML predictions. This distance, termed Δ_{opt}, shows that (with the exception of $\beta = 1$), the NN predicted optimum is closer to the true model than the SVGP or POLY. To assess accuracy in the colormap as a whole, we can take the Root Mean Squared Error (RMSE) between the analytic model and the ML model's colormap values which clearly show lower error for the NN in comparison to the SVGP and POLY.

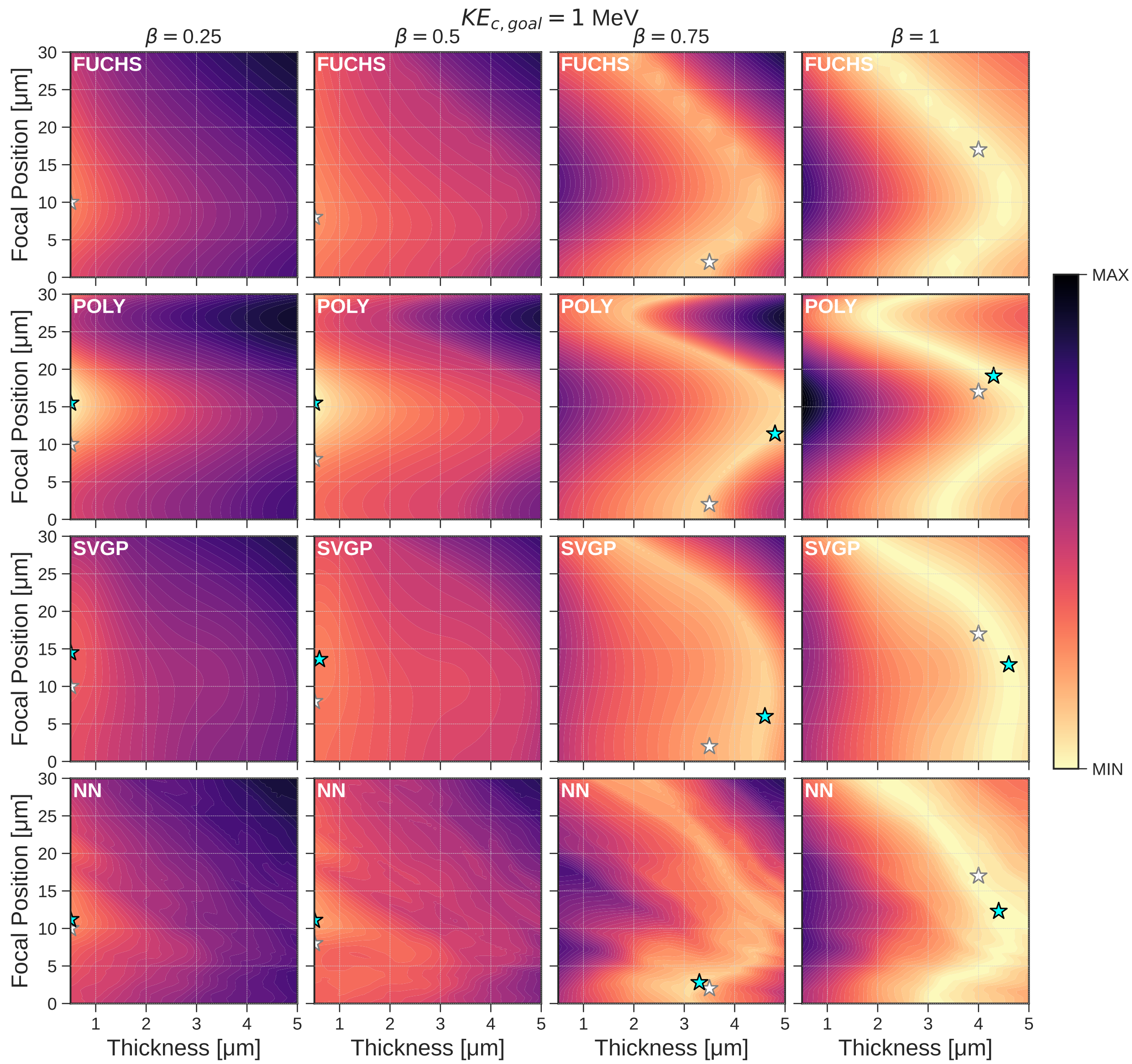

Figure 5.12: Colormaps that show estimates of Equation 5.32 assuming $KE_{\mathrm{c,goal}} = 1$ MeV for the three ML models (NN, POLY and SVGP) and the modified Fuchs et al. model dataset with no added noise (FUCHS). The modified Fuchs et al. model with added 30% Gaussian noise was used to produce the training data for the ML models. For each β value (i.e. each column), the same color levels are used in order to facilitate comparison between the models. A cyan colored star is placed at the location where each ML model predicts a minimum value for Equation 5.32 which can be compared to the analytic model prediction indicated by a white star.

5.3.4 Constrained Data Campaign

Earlier, we describe how synthetic data was generated using a uniform grid in multiple dimensions of laser and target parameters. This scheme was how the primary training set data for the ML models discussed in the main body of the paper was obtained. From an experimental point of view, this approach is not very realistic because a real laser system will scan through the laser and target parameters in a very specific way with specific choices, for example, about which parameters to vary first, while keeping other parameters constant, and which parameters to vary later while keeping other parameters constant. How do these choices affect the accuracy of ML models trained on this data? This is a question that we cannot yet answer conclusively, but we include an investigation into two realistic parameter scans (a.k.a. "campaigns") that are used to train ML models instead of the uniform grid approach.

As highlighted in Figure 5.13, there were two experimental "campaigns" that were used to produce synthetic data – one where thickness, focal depth and laser energy were varied assuming low pre-pulse contrast (10^{-7}), and another where thickness, laser energy and pre-pulse contrast were varied between 10^{-7} and 10^{-6}. All the synthetic data from the two campaigns were used to train ML models. In this way, our training set includes variation in four different input parameters.

The first campaign was generated by stepping through thickness-intensity coordinates, incrementing the focal distance by 3 µm and the thickness by 0.05 µm, performing a full scan of focal depth values at 0.5 µm and every integer value until 5.0 µm. At each point along the thickness-intensity curve, a full sweep of intensity was performed. Since, in a real experiment, the intensity can be controlled by varying a polarizing wave plate, the synthetic data set for this investigation varied the intensity by multiplying the maximum intensity value (10^{19} W cm^{-2}) by the cosine-squared of the wave plate angle, which was varied from 0° to 70° and back over the course of an intensity sweep. The resulting sweep is depicted in Figure 5.13a, creating a set of 1.15 million data points.

The second campaign was generated in a similar manner, but because, in a real experiment, neither main pulse nor pre-pulse laser intensity have an appreciable effect on target stability, both were able to be varied simultaneously. As such, the data set was generated by incrementing thickness by 0.05 µm from 0.5 to 5.0 µm, taking a full scan of both main pulse intensity and contrast at every thickness value. The pre-pulse contrast was varied in the same manner as the main pulse intensity, so the contrast was varied according to a cosine-squared function of another angle. The resulting data are depicted in Figure 5.13b, with an overall size of 1.27 million data points.

In both campaigns, choices about how many increments to make for different parameters were influenced by a constraint that each campaign last no more than about an hour on a 1 kHz repetition rate laser system. Both campaigns assumed 10% added gaussian noise,

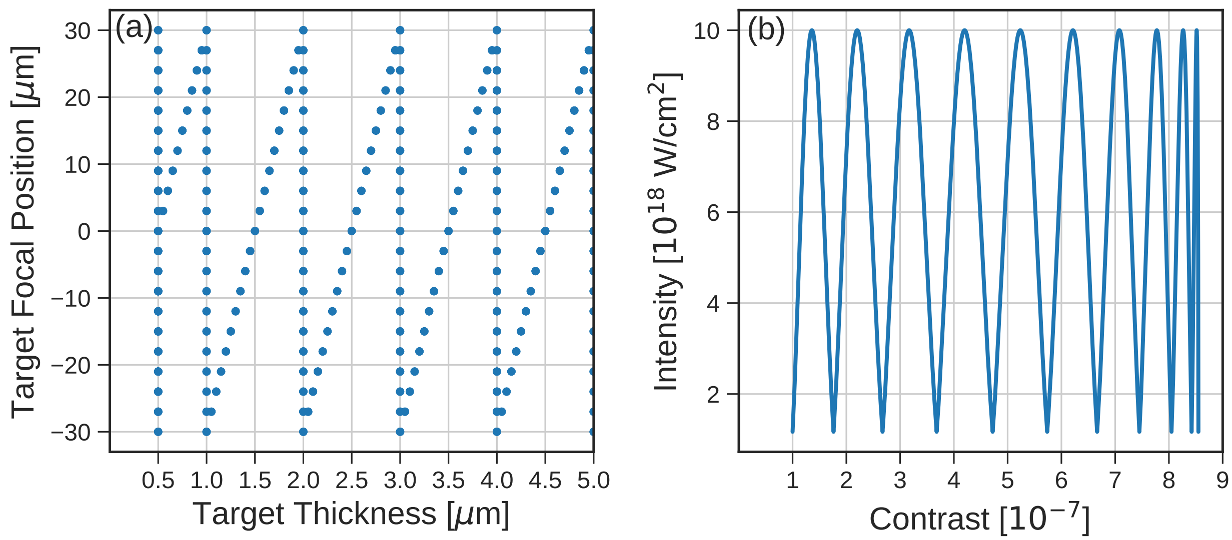

Figure 5.13: Synthetic data was generated in one of two “campaigns”. In (a) campaign 1, the target focus and thickness is varied in discrete steps and each blue dot varies the laser energy from minimum to maximum. In (b) campaign 2, the depicted intensity and contrast looping is performed for discrete steps in target thickness from 0.5 μm to 5μm

following the same prescription used in both section 5.2 and section 5.3. The combined training set, which includes data from both campaigns, has a total size of 2.42 million data points. To better compare with earlier results shown in Figure 5.9a in which the ML models were trained with different numbers of training points, we randomly sampled from this data set. To test the accuracy of the trained ML mdoels, we use the same testing set utilized in Figure 5.9a, which did not include any noise. Our results are shown in Figure 5.14.

Figure 5.14 shows that, overall, the NN and SVGP models have a much higher MAPE than was seen earlier in Figure 5.9a. As shown in Figure 5.14, a third order polynomial fits the data set almost as well as NN and SVGP which indicates that the NN and SVGP models are not able to fit the underlying model very well when trained on data split into two the campaigns we described. A possible improvement could be an experimental design where both the target focal position and the pre-pulse contrast are varied simultaneously, rather than keeping the contrast fixed and varying the target focal position (first campaign), and then varying the contrast while keeping the target focal position fixed (second campaign). But varying as many as four parameters simultaneously creates its own challenges for exploring a large parameter space in a relatively short amount of time ($\sim$ 1-2 hours).

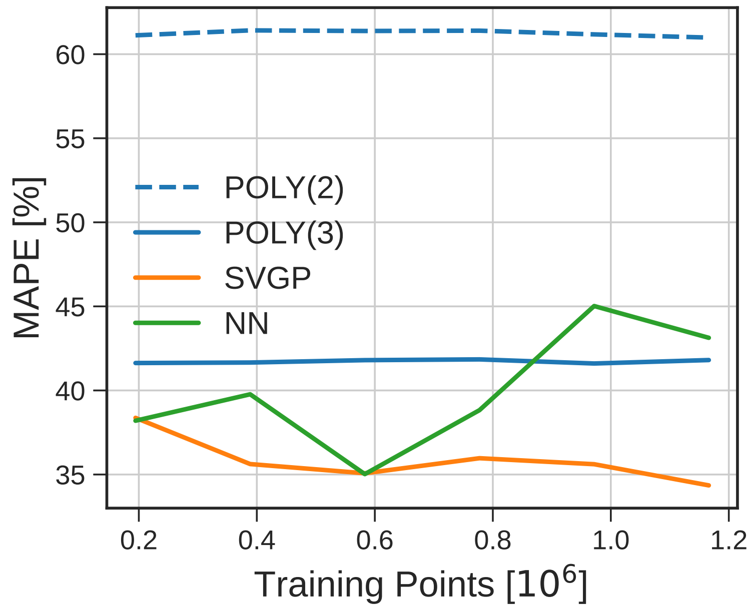

Figure 5.14: Testing set MAPE evaluated on several ML models trained on data combined from two separate campaigns shown in Figure 5.13. The dashed line differs from the solid blue line in the polynomial degree.

The different data splits are chosen to be approximately the same as what was shown in Figure 5.9.

5.4 Conclusion

In section 5.1, we reviewed the physics of the isothermal expansion model for which the Fuchs et al. model is based upon. Then, we showed the modifications that we made to the model to better fit data at the WP-ELL facility and account for pre-expansion of the target. From this modified model, we were well equipped to construct a synthetic dataset that could have multiple inputs/outputs and added noise.

Then, in section 5.2, we summarized our first machine learning effort which analyzed a 25,000 point dataset with three machine learning methods: gaussian process regression, neural networks, and support vector regression. In this work, we generally found that the neural network model was the least accurate and had the worst performance on our optimization task. This was that surprising because neural networks only work well for larger datasets. The gaussian process regression and support vector regression were both similarly accurate; in part, this was due to the relatively simple physics model we used. However, the gaussian process consumed a lot of memory and would be unsuitable for larger datasets.

Next, in section 5.3, we described the second machine learning effort which expanded upon the first by using a dataset of over 1 million points with a more complex model that accounted for an additional input (pre-pulse contrast). We did a similar analyis and found that the added complexity actually made the neural network model a more favorable choice. We used a different implementation of the gaussian process which was capable of handling the million point dataset and achieved good accuracy, but still suffered from long run times. The added complexity also made it difficult for the simpler polynomial model to fit the data.

Throughout this chapter, we explored a novel idea in the field of plasma physics: generating a synthetic dataset based on modifications of established physical models to provide machine learning insights. Our model could, in principle, further be improved to take into account other phenomena that a 1D model could not capture like the shape of the target or the laser angle of incidence. Even though the model may not match up exactly to experiment, it would have the desired trends that we would expect in a real experiment which can at least give us insights into how a hypothetical machine learning framework might operate. By offering the code and synthetic datasets publicly [88, 89], we hope that other researchers in this field can be better prepared to handle the vast amounts of data that future high repetition-rate lasers with continuously refreshing liquid targets can produce. s to train on 1 Million training points on one GPU.

Chapter 6
Optimization and Control of a kHz Laser System

Experimental Layout: charge coupled device (CCD) covered with aluminum which stops low energy protons and ions of lower charge to mass ratio (need to confirm this is true)

6.1 Background

6.2 Methods

6.3 Discussion

Chapter 7
Conclusion

7.1 Summary

7.2 Future Work

Bibliography

[1] Radhe Mohan. A review of proton therapy – current status and future directions. *Precision Radiation Oncology*, 6(2):164–176, 2022.

[2] R. Betti and O. Hurricane. Inertial-confinement fusion with lasers. *Nature Physics*, 12:435–448, May 2016.

[3] Frédéric Boivin, Simon Vallières, Sylvain Fourmaux, Stéphane Payeur, and Patrizio Antici. Quantitative laser-based x-ray fluorescence and particle-induced x-ray emission. *New Journal of Physics*, 24(5):053018, may 2022.

[4] Joseph Richard Harrison Smith. *Advanced Simulations and Optimization of Intense Laser Interactions*. PhD thesis, The Ohio State University, May 2020. Available at http://rave.ohiolink.edu/etdc/view?acc_num=osu1589302684037632.

[5] S. C. Wilks, W. L. Kruer, M. Tabak, and A. B. Langdon. Absorption of ultra-intense laser pulses. *Phys. Rev. Lett.*, 69:1383–1386, Aug 1992.

[6] Paul Gibbon and A. R. Bell. Collisionless absorption in sharp-edged plasmas. *Phys. Rev. Lett.*, 68:1535–1538, Mar 1992.

[7] D. W. Forslund, J. M. Kindel, and K. Lee. Theory of hot-electron spectra at high laser intensity. *Phys. Rev. Lett.*, 39:284–288, Aug 1977.

[8] F. Brunel. Not-so-resonant, resonant absorption. *Phys. Rev. Lett.*, 59:52–55, Jul 1987.

[9] Paul Gibbon. *Short Pulse Laser Interactions with Matter*. Imperial College Press, 2005.

[10] M. Roth and M. S. Schollmeier. Ion acceleration - target normal sheath acceleration. In *Proceedings of the 2014 CAS-CERN Accelerator School: Plasma Wake Acceleration*, volume 1, pages 231–270, 2 2016.

[11] K. V. Lezhnin, F. F. Kamenets, V. S. Beskin, M. Kando, T. Zh. Esirkepov, and S. V. Bulanov. Effect of electromagnetic pulse transverse inhomogeneity on ion acceleration by radiation pressure. *Physics of Plasmas*, 22(3):033112, 03 2015.

[12] K. Markey, P. McKenna, C. M. Brenner, D. C. Carroll, M. M. Günther, K. Harres, S. Kar, K. Lancaster, F. Nürnberg, M. N. Quinn, A. P. L. Robinson, M. Roth, M. Zepf, and D. Neely. Spectral enhancement in the double pulse regime of laser proton acceleration. *Phys. Rev. Lett.*, 105:195008, Nov 2010.

[13] G. G. Scott, J. S. Green, V. Bagnoud, C. Brabetz, C. M. Brenner, D. C. Carroll, D. A. MacLellan, A. P. L. Robinson, M. Roth, C. Spindloe, F. Wagner, B. Zielbauer, P. McKenna, and D. Neely. Multi-pulse enhanced laser ion acceleration using plasma half cavity targets. *Applied Physics Letters*, 101(2):024101, 07 2012.

[14] J. Ferri, E. Siminos, and T. Fülöp. Enhanced target normal sheath acceleration using colliding laser pulses. *Communications Physics*, 2:40, 4 2019.

[15] Weipeng Yao, Motoaki Nakatsutsumi, Sébastien Buffechoux, Patrizio Antici, Marco Borghesi, Andrea Ciardi, Sophia N. Chen, Emmanuel d'Humières, Laurent Gremillet, Robert Heathcote, Vojtěch Horný, Paul McKenna, Mark N. Quinn, Lorenzo Romagnani, Ryan Royle, Gianluca Sarri, Yasuhiko Sentoku, Hans-Peter Schlenvoigt, Toma Toncian, Olivier Tresca, Laura Vassura, Oswald Willi, and Julien Fuchs. Optimizing laser coupling, matter heating, and particle acceleration from solids using multiplexed ultraintense lasers. *Matter and Radiation at Extremes*, 9(4):047202, 04 2024.

[16] P. Mora. Plasma expansion into a vacuum. *Phys. Rev. Lett.*, 90:185002, May 2003.

[17] John J. Felice, Ronak Desai, Nathaniel Tamminga, Joseph R. Smith, Alona Kryshchenko, Chris Orban, Michael L. Dexter, and Anil K. Patnaik. Towards automated learning with ultra-intense laser systems
operating in the khz repetition rate regime, 2025.

[18] John T. Morrison, Scott Feister, Kyle D. Frische, Drake R. Austin, Gregory K. Ngirmang, Neil R. Murphy, Chris Orban, Enam A. Chowdhury, and W. M. Roquemore. MeV proton acceleration at kHz repetition rate from ultra-intense laser liquid interaction. *New Journal of Physics*, 20(2):022001, February 2018.

[19] John J. Felice, Ronak Desai, Nathaniel Tamminga, Joseph R. Smith, Alona Kryshchenko, Chris Orban, Michael L. Dexter, and Anil K. Patnaik. Towards automated learning with ultra-intense laser systems
operating in the khz repetition rate regime. *Contributions to Plasma Physics*, page e202400080, 2024.

[20] Mayo Clinic Staff. Radiation therapy, 2024. https://www.mayoclinic.org/tests-procedures/radiation-therapy/about/pac-20385162.

[21] W. H. Bragg and R. Kleeman. Xxxix. on the particles of radium, and their loss of range in passing through various atoms and molecules. *The London, Edinburgh, and Dublin Philosophical Magazine and Journal of Science*, 10(57):318–340, 1905.

[22] Robert R. Wilson. Radiological use of fast protons. *Radiology*, 47(5):487–491, 1946. PMID: 20274616.

[23] James F. Ziegler, M.D. Ziegler, and J.P. Biersack. Srim – the stopping and range of ions in matter (2010). *Nuclear Instruments and Methods in Physics Research Section B: Beam Interactions with Materials and Atoms*, 268(11):1818–1823, 2010. 19th International Conference on Ion Beam Analysis.

[24] https://cancer.osu.edu/for-patients-and-caregivers/learn-about-cancers-and-treatments/clinical-services-at-the-james/radiation-oncology/treatment/proton-therapy. Accessed: 2024-12-19.

[25] Ute Linz and Jose Alonso. Laser-driven ion accelerators for tumor therapy revisited. *Phys. Rev. Accel. Beams*, 19:124802, Dec 2016.

[26] Derek B. Schaeffer, Archie F. A. Bott, Marco Borghesi, Kirk A. Flippo, William Fox, Julien Fuchs, Chikang Li, Fredrick H. Séguin, Hye-Sook Park, Petros Tzeferacos, and Louise Willingale. Proton imaging of high-energy-density laboratory plasmas. *Rev. Mod. Phys.*, 95:045007, Dec 2023.

[27] R A Simpson, D A Mariscal, J Kim, G G Scott, G J Williams, E Grace, C McGuffey, S Wilks, A Kemp, N Lemos, B Z Djordjevic, E Folsom, D Kalantar, R Zacharias, B Pollock, J Moody, F Beg, A Morace, N Iwata, Y Sentoku, M J-E Manuel, M Mauldin, M Quinn, K Youngblood, M Gatu-Johnson, B Lahmann, C Haefner, D Neely, and T Ma. Demonstration of tnsa proton radiography on the national ignition facility advanced radiographic capability (nif-arc) laser. *Plasma Physics and Controlled Fusion*, 63(12):124006, nov 2021.

[28] A. B. Zylstra, C. K. Li, H. G. Rinderknecht, F. H. Séguin, R. D. Petrasso, C. Stoeckl, D. D. Meyerhofer, P. Nilson, T. C. Sangster, S. Le Pape, A. Mackinnon, and P. Patel. Using high-intensity laser-generated energetic protons to radiograph directly driven implosions. *Review of Scientific Instruments*, 83(1):013511, 01 2012.

[29] M. Passoni, L. Fedeli, and F. Mirani. Superintense laser-driven ion beam analysis. *Scientific Reports*, 9, JUN 24 2019.

[30] F.F. Chen. *Introduction to Plasma Physics and Controlled Fusion*. Springer, 3 edition, 2015.

[31] Andrew Zangwill. *Modern Electrodynamics*. Cambridge University Press, 2012.

[32] Andrea Macchi. *A Superintense Laser-Plasma Interaction Theory Primer*. Springer, 2013.

[33] William Kruer. *The Physics of Laser Plasma Interactions*. CRC Press, 2003.

[34] N. G. Denisov. On a singularity of the field of an electromagnetic wave propagated in an inhomogeneous plasma. *Soviet Physics JETP*, 4(4):544–553, 5 1957.

[35] D. W. Forslund, J. M. Kindel, Kenneth Lee, E. L. Lindman, and R. L. Morse. Theory and simulation of resonant absorption in a hot plasma. *Phys. Rev. A*, 11:679–683, Feb 1975.

[36] J. P. Freidberg, R. W. Mitchell, R. L. Morse, and L. I. Rudsinski. Resonant absorption of laser light by plasma targets. *Phys. Rev. Lett.*, 28:795–799, Mar 1972.

[37] K. G. Estabrook, E. J. Valeo, and W. L. Kruer. Two-dimensional relativistic simulations of resonance absorption. *The Physics of Fluids*, 18(9):1151–1159, 09 1975.

[38] M. K. Grimes, A. R. Rundquist, Y.-S. Lee, and M. C. Downer. Experimental identification of “vacuum heating” at femtosecond-laser-irradiated metal surfaces. *Phys. Rev. Lett.*, 82:4010–4013, May 1999.

[39] P. B. Corkum. Plasma perspective on strong field multiphoton ionization. *Phys. Rev. Lett.*, 71:1994–1997, Sep 1993.

[40] NobelPrize.org. Press release, 2023.

[41] David J. Griffiths. *Introduction to Electrodynamics*. Cambridge University Press, 4 edition, 2017.

[42] W. L. Kruer and Kent Estabrook. J×b heating by very intense laser light. *The Physics of Fluids*, 28(1):430–432, 01 1985.

[43] A. Macchi, M. Borghesi, and M. Passoni. Ion acceleration by superintense laser-plasma interaction. *Rev. Mod. Phys.*, 85:751–793, May 2013.

[44] T. H. Tan, G. H. McCall, and A. H. Williams. Determination of laser intensity and hot-electron temperature from fastest ion velocity measurement on laser-produced plasma. *The Physics of Fluids*, 27(1):296–301, 01 1984.

[45] S. J. Gitomer, R. D. Jones, F. Begay, A. W. Ehler, J. F. Kephart, and R. Kristal. Fast ions and hot electrons in the laser–plasma interaction. *The Physics of Fluids*, 29(8):2679–2688, 08 1986.

[46] M. Allen, P. K. Patel, A. Mackinnon, D. Price, S. Wilks, and E. Morse. Direct experimental evidence of back-surface ion acceleration from laser-irradiated gold foils. *Phys. Rev. Lett.*, 93:265004, Dec 2004.

[47] J. E. Crow, P. L. Auer, and J. E. Allen. The expansion of a plasma into a vacuum. *Journal of Plasma Physics*, 14(1):65–76, 1975.

[48] Yasuaki Kishimoto, Kunioki Mima, Tsuguhiro Watanabe, and Kyoji Nishikawa. Analysis of fast-ion velocity distributions in laser plasmas with a truncated Maxwellian velocity distribution of hot electrons. *The Physics of Fluids*, 26(8):2308–2315, 08 1983.

[49] Donna Strickland and Gerard Mourou. Compression of amplified chirped optical pulses. *Optics Communications*, 56(3):219–221, 1985.

[50] NobelPrize.org. Press release, 2018.

[51] A. Maksimchuk, S. Gu, K. Flippo, D. Umstadter, and V. Yu. Bychenkov. Forward ion acceleration in thin films driven by a high-intensity laser. *Phys. Rev. Lett.*, 84:4108–4111, May 2000.

[52] E. L. Clark, K. Krushelnick, M. Zepf, F. N. Beg, M. Tatarakis, A. Machacek, M. I. K. Santala, I. Watts, P. A. Norreys, and A. E. Dangor. Energetic heavy-ion and proton generation from ultraintense laser-plasma interactions with solids. *Phys. Rev. Lett.*, 85:1654–1657, Aug 2000.

[53] R. A. Snavely, M. H. Key, S. P. Hatchett, T. E. Cowan, M. Roth, T. W. Phillips, M. A. Stoyer, E. A. Henry, T. C. Sangster, M. S. Singh, S. C. Wilks, A. MacKinnon, A. Offenberger, D. M. Pennington, K. Yasuike, A. B. Langdon, B. F. Lasinski, J. Johnson, M. D. Perry, and E. M. Campbell. Intense high-energy proton beams from petawatt-laser irradiation of solids. *Phys. Rev. Lett.*, 85:2945–2948, Oct 2000.

[54] S. C. Wilks, A. B. Langdon, T. E. Cowan, M. Roth, M. Singh, S. Hatchett, M. H. Key, D. Pennington, A. MacKinnon, and R. A. Snavely. Energetic proton generation in ultra-intense laser–solid interactions. *Physics of Plasmas*, 8(2):542–549, 02 2001.

[55] C. Perego, A. Zani, D. Batani, and M. Passoni. Extensive comparison among target normal sheath acceleration theoretical models. *Nuclear Instruments and Methods in Physics Research Section A: Accelerators, Spectrometers, Detectors and Associated Equipment*, 653(1):89–93, 2011. Superstrong 2010.

[56] P. Mora. Thin-foil expansion into a vacuum. *Phys. Rev. E*, 72:056401, Nov 2005.

[57] M. Passoni and M. Lontano. One-dimensional model of the electrostatic ion acceleration in the ultraintense laser–solid interaction. *Laser and Particle Beams*, 22(2):163–169, 2004.

[58] Maurizio Lontano and Matteo Passoni. Electrostatic field distribution at the sharp interface between high density matter and vacuum. *Physics of Plasmas*, 13(4):042102, 04 2006.

[59] M. Passoni and M. Lontano. Theory of light-ion acceleration driven by a strong charge separation. *Phys. Rev. Lett.*, 101:115001, Sep 2008.

[60] C. Perego, D. Batani, A. Zani, and M. Passoni. Target normal sheath acceleration analytical modeling, comparative study and developmentsa). *Review of Scientific Instruments*, 83(2):02B502, 02 2012.

[61] A. P. L Robinson, A. R. Bell, and R. J. Kingham. Effect of target composition on proton energy spectra in ultraintense laser-solid interactions. *Phys. Rev. Lett.*, 96:035005, Jan 2006.

[62] B. J. Albright, L. Yin, B. M. Hegelich, Kevin J. Bowers, T. J. T. Kwan, and J. C. Fernández. Theory of laser acceleration of light-ion beams from interaction of ultrahigh-intensity lasers with layered targets. *Phys. Rev. Lett.*, 97:115002, Sep 2006.

[63] P. K. Patel, A. J. Mackinnon, M. H. Key, T. E. Cowan, M. E. Foord, M. Allen, D. F. Price, H. Ruhl, P. T. Springer, and R. Stephens. Isochoric heating of solid-density matter with an ultrafast proton beam. *Phys. Rev. Lett.*, 91:125004, Sep 2003.

[64] A. J. Mackinnon, Y. Sentoku, P. K. Patel, D. W. Price, S. Hatchett, M. H. Key, C. Andersen, R. Snavely, and R. R. Freeman. Enhancement of proton acceleration by hot-electron recirculation in thin foils irradiated by ultraintense laser pulses. *Phys. Rev. Lett.*, 88:215006, May 2002.

[65] S. Vallieres. Enhanced laser-driven proton acceleration using nanowire targets. *Scientific Reports*, 11, 1 2021.

[66] Joseph. Strehlow. A laser parameter study on enhancing proton generation from microtube foil targets. *Scientific Reports*, 12, 6 2022.

[67] P. McKenna, D.C. Carroll, O. Lundh, F. Nürnberg, K. Markey, S. Bandyopadhyay, D. Batani, R.G. Evans, R. Jafer, S. Kar, and et al. Effects of front surface plasma expansion on proton acceleration in ultraintense laser irradiation of foil targets. *Laser and Particle Beams*, 26(4):591–596, 2008.

[68] J. Ferri, L. Senje, M. Dalui, K. Svensson, B. Aurand, M. Hansson, A. Persson, O. Lundh, C.-G. Wahlström, L. Gremillet, E. Siminos, T. C. DuBois, L. Yi, J. L. Martins, and T. Fülöp. Proton acceleration by a pair of successive ultraintense femtosecond laser pulses. *Physics of Plasmas*, 25(4):043115, 04 2018.

[69] J. Fuchs, P. Antici, E. D'Humières, E. Lefebvre, M. Borghesi, E. Brambrink, C. Cecchetti, M. Kaluza, V. Malka, M. Manclossi, S. Meyroneinc, P. Mora, J. Schreiber, T. Toncian, H. Pépin, and P. Audebert. Laser-driven proton scaling laws and new paths towards energy increase. *Nature Physics*, 2, 12 2005.

[70] T. Tajima and J. M. Dawson. Laser electron accelerator. *Phys. Rev. Lett.*, 43:267–270, Jul 1979.

[71] E. Esarey, C. B. Schroeder, and W. P. Leemans. Physics of laser-driven plasma-based electron accelerators. *Rev. Mod. Phys.*, 81:1229–1285, Aug 2009.

[72] C.K. Birdsall and A.B. Langdon. *Plasma Physics Via Computer Simulation*. Series In Plasma Physics. Taylor & Francis, 2004.

[73] T D Arber, K Bennett, C S Brady, A Lawrence-Douglas, M G Ramsay, N J Sircombe, P Gillies, R G Evans, H Schmitz, A R Bell, and C P Ridgers. Contemporary particle-in-cell approach to laser-plasma modelling. *Plasma Physics and Controlled Fusion*, 57(11):113001, sep 2015.

[74] D.R. Welch, D.V. Rose, R.E. Clark, T.C. Genoni, and T.P. Hughes. Implementation of an non-iterative implicit electromagnetic field solver for dense plasma simulation. *Computer Physics Communications*, 164(1):183–188, 2004. Proceedings of the 18th International Conferene on the Numerical Simulation of Plasmas.

[75] J. Fuchs, C. A. Cecchetti, M. Borghesi, T. Grismayer, E. d'Humières, P. Antici, S. Atzeni, P. Mora, A. Pipahl, L. Romagnani, A. Schiavi, Y. Sentoku, T. Toncian, P. Audebert, and O. Willi. Laser-foil acceleration of high-energy protons in small-scale plasma gradients. *Phys. Rev. Lett.*, 99:015002, Jul 2007.

[76] A P L Robinson, D Neely, P McKenna, and R G Evans. Spectral control in proton acceleration with multiple laser pulses. *Plasma Physics and Controlled Fusion*, 49(4):373, feb 2007.

[77] Nashad Rahman, Joseph R. Smith, Gregory K. Ngirmang, and Chris Orban. Particle-in-cell modeling of a potential demonstration experiment for double pulse enhanced target normal sheath acceleration. *Physics of Plasmas*, 28(7):073103, 07 2021.

[78] Imran Khan and Vikrant Saxena. Tnsa based proton acceleration by two oblique laser pulses in the presence of an axial magnetic field. *New Journal of Physics*, 26(8):083026, aug 2024.

[79] A Arefiev, T Toncian, and G Fiksel. Enhanced proton acceleration in an applied longitudinal magnetic field. *New Journal of Physics*, 18(10):105011, oct 2016.

[80] A. Morace, N. Iwata, and Y. Sentoku. Enhancing laser beam performance by interfering intense laser beamlets. *Nat Commun*, 10:2995, 7 2019.

[81] Adam Paszke, Sam Gross, Francisco Massa, Adam Lerer, James Bradbury, Gregory Chanan, Trevor Killeen, Zeming Lin, Natalia Gimelshein, Luca Antiga, Alban Desmaison, Andreas Kopf, Edward Yang, Zachary DeVito, Martin Raison, Alykhan Tejani, Sasank Chilamkurthy, Benoit Steiner, Lu Fang, Junjie Bai, and Soumith Chintala. Pytorch: An imperative style, high-performance deep learning library. In H. Wallach, H. Larochelle, A. Beygelzimer, F. d'Alché-Buc, E. Fox, and R. Garnett, editors, *Advances in Neural Information Processing Systems*, volume 32. Curran Associates, Inc., 2019.

[82] Sören Jalas, Manuel Kirchen, Philipp Messner, Paul Winkler, Lars Hübner, Julian Dirkwinkel, Matthias Schnepp, Remi Lehe, and Andreas R. Maier. Bayesian optimization of a laser-plasma accelerator. *Phys. Rev. Lett.*, 126:104801, Mar 2021.

[83] E J Dolier, M King, R Wilson, R J Gray, and P McKenna. Multi-parameter bayesian optimisation of laser-driven ion acceleration in particle-in-cell simulations. *New Journal of Physics*, 24(7):073025, jul 2022.

[84] B. Loughran, M. J. V. Streeter, H. Ahmed, S. Astbury, M. Balcazar, M. Borghesi, N. Bourgeois, C. B. Curry, S. J. D. Dann, S. DiIorio, and et al. Automated control and optimization of laser-driven ion acceleration. *High Power Laser Science and Engineering*, 11:e35, 2023.

[85] B Z Djordjević, A J Kemp, J Kim, J Ludwig, R A Simpson, S C Wilks, T Ma, and D A Mariscal. Characterizing the acceleration time of laser-driven ion acceleration with data-informed neural networks. *Plasma Physics and Controlled Fusion*, 63(9):094005, aug 2021.

[86] B. Schmitz, D. Kreuter, O. Boine-Frankenheim, and Daniele Margarone. Modeling of a liquid leaf target tnsa experiment using particle-in-cell simulations and deep learning. *Laser and Particle Beams*, 2023:e3, 2023.

[87] K. M. George, J. T. Morrison, S. Feister, G. K. Ngirmang, J. R. Smith, A. J. Klim, J. Snyder, D. Austin, W. Erbsen, K. D. Frische, and et al. High-repetition-rate ($\geqslant$ khz)

targets and optics from liquid microjets for high-intensity laser–plasma interactions. *High Power Laser Science and Engineering*, 7:e50, 2019.

[88] Ronak Desai. Datasets and code from "applying machine learning methods to laser acceleration of protons: lessons learned from synthetic data". https://doi.org/10.5281/zenodo.12752264, July 2024.

[89] Ronak Desai and John J. Felice. Datasets and code from "towards automated learning with ultra-intense laser systems operating in the khz repetition rate regime", October 2024.

[90] M. Passoni, L. Bertagna, and A. Zani. Target normal sheath acceleration: theory, comparison with experiments and future perspectives. *New Journal of Physics*, 12(4):045012, apr 2010.

[91] J. Schreiber, F. Bell, F. Grüner, U. Schramm, M. Geissler, M. Schnürer, S. Ter-Avetisyan, B. M. Hegelich, J. Cobble, E. Brambrink, J. Fuchs, P. Audebert, and D. Habs. Analytical model for ion acceleration by high-intensity laser pulses. *Phys. Rev. Lett.*, 97:045005, Jul 2006.

[92] M. H. Key, M. D. Cable, T. E. Cowan, K. G. Estabrook, B. A. Hammel, S. P. Hatchett, E. A. Henry, D. E. Hinkel, J. D. Kilkenny, J. A. Koch, W. L. Kruer, A. B. Langdon, B. F. Lasinski, R. W. Lee, B. J. MacGowan, A. MacKinnon, J. D. Moody, M. J. Moran, A. A. Offenberger, D. M. Pennington, M. D. Perry, T. J. Phillips, T. C. Sangster, M. S. Singh, M. A. Stoyer, M. Tabak, G. L. Tietbohl, M. Tsukamoto, K. Wharton, and S. C. Wilks. Hot electron production and heating by hot electrons in fast ignitor research. *Physics of Plasmas*, 5(5):1966–1972, 05 1998.

[93] C. D. Decker, W. B. Mori, K.-C. Tzeng, and T. Katsouleas. The evolution of ultra-intense, short-pulse lasers in underdense plasmas. *Physics of Plasmas*, 3(5):2047–2056, 05 1996.

[94] Don M. Miller. Reducing transformation bias in curve fitting. *The American Statistician*, 38(2):124–126, 1984.

[95] RAPIDS Development Team. *RAPIDS: Libraries for End to End GPU Data Science*, 2023.

[96] Jacob R Gardner, Geoff Pleiss, David Bindel, Kilian Q Weinberger, and Andrew Gordon Wilson. Gpytorch: Blackbox matrix-matrix gaussian process inference with gpu acceleration. In *Advances in Neural Information Processing Systems*, 2018.

[97] Marian Tietz, Thomas J. Fan, Daniel Nouri, Benjamin Bossan, and skorch Developers. *skorch: A scikit-learn compatible neural network library that wraps PyTorch*, July 2017.

[98] Ke Alexander Wang, Geoff Pleiss, Jacob R. Gardner, Stephen Tyree, Kilian Q. Weinberger, and Andrew Gordon Wilson. Exact gaussian processes on a million data points, 2019.

[99] James Hensman, Alex Matthews, and Zoubin Ghahramani. Scalable variational gaussian process classification, 2014.

[100] R.W. Hockney and J.W. Eastwood. *Computer Simulation Using Particles*. CRC Press, 1988.

[101] R.W Hockney. Measurements of collision and heating times in a two-dimensional thermal computer plasma. *Journal of Computational Physics*, 8(1):19–44, 1971.

[102] D.C. Montgomery and D.A. Tidman. *Plasma Kinetic Theory*. McGraw-Hill advanced physics monograph series. McGraw-Hill, 1964.

Appendix A
Energy Conservation in EPOCH Particle-in-Cell Simulations Due to Finite Numbers of Particles

This appendix focuses on unpublished work that was done jointly with Ricky Oropeza and Joseph Smith. My contributions to this project were primarily done as a pre-candidacy student.

PIC simulations provide a useful but imperfect model of various plasma phenomena. In this work, the impact of the finite number of particles in a PIC simulation on the energy conservation is considered and explored through ultra-intense laser interactions with a thin, near solid density target in the TNSA regime.

A.1 Background

Explicit PIC codes tend to gain energy over time through what can be attributed as numerical errors. In this section, we consider which plasma and simulation parameters affect this numerical energy gain and derive various scalings.

A.1.1 Electric Field Fluctuations

In PIC simulations, we compute the velocities at the next timestep through eq. (3.12) which is dependent on the time-step Δt. Due to using a finite grid, approximating real particles with macro particles, and using a finite Δt, we will develop some errors in calculating the electric field δE. The corresponding force miscalculation $\delta F = q\delta E\Delta t$ would deliver an impulse $m\delta v$ and result in a velocity difference [100] of

$$\delta v = \frac{q}{m}\Delta t\delta E \tag{A.1}$$

We can make an assumption that these field calculation errors will be randomly distributed which can be treated as a random walk in velocity space. If we consider Δv as the total deviation of the calculated velocity from the true value, we should expect $\langle \Delta v \rangle = 0$ due to the symmetry of this random walk. However, the squared deviations on average will increase over time; for n time-steps (each with the same random error δE), we would have

$$\langle \Delta v^2 \rangle = n\delta v^2 = n\frac{q^2}{m^2}\Delta t^2 \delta E^2 \tag{A.2}$$

We can see that the average change in kinetic energy $\Delta KE \equiv \frac{1}{2}m\langle v^2 \rangle$ increases linearly with the number of time-steps n [100]. Additionally, since $\Delta KE \propto \frac{1}{m}$, the heavier particles (i.e. ions) can usually be neglected when examining the artificial heating [100]. Hockney postulates a related expression [101] for ΔKE in another work as

$$\Delta KE \sim \frac{q^2}{m}\langle E^2 \rangle \tau_{\text{corr}} \Delta t \tag{A.3}$$

where τ_{corr} can be identified with the period of plasma oscillations $\sim \omega_{p,e}^{-1}$. Then, expressing the charge of one electron macro-particle as $q = e\frac{N}{N_{mac}} = \frac{en}{n_{mac}} = \frac{en\Delta x^2}{n_{ppc}}$, where Δx is the cell size and n_{ppc} is the number of electron macro-particles per cell, the kinetic energy increase becomes

$$\Delta KE = (\frac{e}{m_e})\frac{en\Delta x^2}{n_{ppc}}\langle E^2 \rangle \frac{2\pi}{\omega_{pe}}\Delta t \tag{A.4}$$

Hockney uses a result from Chapter 8.2 of Montgomery and Tidman [102] for the squared electric field fluctuations

$$\frac{\langle E^2 \rangle}{8\pi} = \frac{k_B T}{2}\int\int_{-\infty}^{+\infty} \frac{dk_x dk_y}{(2\pi)^2}\frac{1}{(1+(k_x^2+k_y^2)\lambda_D^2)} \tag{A.5}$$

which can be solved by letting $u = k\lambda_D$ where $k = \sqrt{k_x^2 + k_y^2}$ and integrating with respect to the polar area element $k\ dk\ d\phi$

$$\langle E^2 \rangle = \frac{k_B T}{4\pi\epsilon_0 \lambda_D^2}\text{Log}(1 + u_{max^2}) \tag{A.6}$$

Here, $u_{max} = k_{\max}\lambda_D$ corresponds to the maximum wavenumber $k_{max} = \frac{2\pi}{\Delta x}$ considered which is limited by the resolution.

A.1.2 Empirical Heating Estimates

Using eqs. (2.15) and (2.17), ΔKE can now be expressed as

$$\Delta KE = \frac{n_e^{3/2}\Delta x^2}{n_{ppc}}\text{Log}(1 + u_{max}^2) \tag{A.7}$$

A more empirical estimate for the heating can be obtained by asserting a general scaling of the heating time $\tau_H \simeq \frac{n_{\text{ppc}}^{\alpha}}{\omega_{p,e}} \left(\frac{\lambda_{D,0}}{\Delta x}\right)^d$, where d and α are constants that can be fit empirically through simulations. If we assert that the linear energy increase $\frac{dT}{dt} = T_0/\tau_H$, we develop a formula (again using eqs. (2.15) and (2.17)) for the linear energy increase

$$\frac{dT_{eV}}{dt_{ps}} = C_H \frac{T_{0,eV}^{1-d/2} \Delta x_{nm}^d n_{23}^{(d+1)/2}}{n_{\text{ppc}}^{\alpha}} \tag{A.8}$$

and when $\alpha = 1$ and $d = 2$, we obtain eq. (30) from Arber et al. [73]

$$\frac{dT_{eV}}{dt_{ps}} = C_H \frac{\Delta x_{nm}^2 n_{23}^{3/2}}{n_{\text{ppc}}} \tag{A.9}$$

where C_H is a constant determined by the shape function and the use of current smoothing. The cell size, number density, time, and temperature are expressed in nm, 10^{23}cm^{-3}, ps, and eV due to being convenient units for PIC simulations. A more sophisticated empirical model could also account for two dimensionless timescales: $\omega_{p,e}\Delta t$ and $v_{\text{th}}\Delta t$, but Hockney [101] notes that these can be ignored by constraining $\omega_{p,e}\Delta t$ to be $\omega_{p,e}\Delta t = \min((2\lambda_D/\Delta x)^{-1}, 1)$ [101].

A.2 Methods

A.3 Conclusion